
A HYBRID QUANTUM-CLASSICAL CFD METHODOLOGY WITH BENCHMARK HHL SOLUTIONS

Leigh Lapworth

Rolls-Royce plc
Derby, UK
June 2, 2022

leigh.lapworth@rolls-royce.com

ABSTRACT

There has been significant progress in the development of quantum algorithms for solving linear systems of equations with a growing body of applications to Computational Fluid Dynamics (CFD) and CFD-like problems. This work extends previous work by developing a non-linear hybrid quantum-classical CFD solver and using it to generate fully converged solutions. The hybrid solver uses the SIMPLE CFD algorithm, which is common in many industrial CFD codes, and applies it to the 2-dimensional lid driven cavity test case. A theme of this work is the classical processing time needed to prepare the quantum circuit with a focus on the decomposition of the CFD matrix into a linear combination of unitaries (LCU). CFD meshes with up to 65×65 nodes are considered with the largest producing a LCU containing 32,767 Pauli strings. A new method for rapidly re-computing the coefficients in a LCU is proposed, although this reduces, rather than eliminates, the classical scaling issues. The quantum linear equation solver uses the Harrow, Hassidim, Lloyd (HHL) algorithm via a state-vector emulator. Test matrices are sampled from the classical CFD solver to investigate the solution accuracy that can be achieved with HHL. For the smallest 5×5 and 9×9 CFD meshes, full non-linear hybrid CFD calculations are performed. The impacts of approximating the LCU and the varying the number of ancilla rotations in the eigenvalue inversion circuit are studied. Preliminary timing results indicate that the classical computer preparation time needed for a hybrid solver is just as important to the achievement of quantum advantage in CFD as the time on the quantum computer. The reported HHL solutions and LCU decompositions provide a benchmark for future research. The CFD test matrices used in this study are available upon request.

1 Introduction

Simulation and modelling, enabled by high performance computing, have transformed the way products are designed and engineered. Successive reports and studies, e.g. [1], have identified computational modelling as a crucial enabler to national productivity and competitiveness. Principle amongst these tools is Computational Fluid Dynamics (CFD) whose uses range from designing widgets on a laptop to simulating the flow through gas turbines using classical supercomputers [2, 3, 4, 5].

Whilst the equations governing CFD are highly nonlinear, many solvers adopt a two layer approach where an outer non-linear step is used to linearise the equations for an inner linear equation solver [6]. This makes CFD attractive for quantum computing particularly for large scale applications which consume huge amounts of classical computing resources in solving the linearised equations.

Previous quantum CFD research includes [7] in which the Quantum Fourier Transform was applied to the Poisson solver within a vortex in-cell method. The resulting hybrid methodology was simulated on a parallel computer using 8 processors to model colliding vortex rings on a 128^3 mesh. [8] emulated the quantum ODE algorithm of [9] to model the 1D flow through a Laval nozzle, demonstrating identical quantum and classical solutions. [10] modelled the 1D

and 2D wave equations using emulated Hamiltonian simulations. [11] extended the simulation of the wave equation to include the design of circuits that were run on an ATOS QLM. [12] used the IBM Qiskit emulator to model the 1D heat conduction equation with 4 mesh points using the HHL algorithm [13]. [14] developed a machine learning approach based on differential quantum circuits and simulated its application to the flow in a convergent-divergent 1D nozzle. Of note is [15] where a variational algorithm was used to develop a NISQ era algorithm for solving Burger's equation on the 20 qubit IBM quantum computers Tokyo and Poughkeepsie. This is one of the few studies to solve a CFD type equation on a physical device. [16] used the Lattice Boltzmann method (LBM) to solve the stream-function (ψ) vorticity (ω) formulation of the Navier-Stokes equation. The circuits followed the evolution of the LBM which does not require the solution of matrix equations. The input state was encoded using the components of (ψ) and (ω) along the lattice directions, resulting in diagonal collision and propagation operators and a simple unitary decomposition. The 2D lid driven was solved for a 16x16 mesh and required a total of 15 qubits using IBM Qiskit in emulation mode.

More generally, significant progress has been made on Quantum Linear Equation Solvers (QLES) since the HHL (Harrow-Hassidim-Lloyd) algorithm was published in 2009 [13]. As in [17], the Lie-Trotter formulae [18] or higher order Suzuki formulae [19] are used to reduce the commutation errors in approximating the exponentiation of the matrix of interest as a product of exponentiated unitaries. Qubitisation techniques [20, 21, 22, 23, 24, 25] provide an exact implementation of a unitary decomposition of the matrix of interest at the expense of an additional ancilla register for *preparing* the coefficients of the unitary decomposition. The prepare register is of size $\log_2(M)$ where M is the number of unitaries in the linear decomposition:

$$H = \sum_{j=1}^M \alpha_j U_j \quad (1)$$

[24] demonstrated a qubitised phase estimation implementation using a block-encoded walk operator as a qubiterate. At the end of the phase estimation the clock register contains an estimate of $\sin^{-1}(\frac{\lambda}{s})$ or $\pi - \sin^{-1}(\frac{\lambda}{s})$ for the eigenvalues λ , where s is the sum of the unitary coefficients which are made positive by taking any negative signs into the unitaries. Whilst this formulation could be implemented within the HHL algorithm, a more promising avenue is Quantum Singular Value Transformation (QSVT) [26, 27, 28] where the matrix is directly inverted using an operator that approximates $1/x$ and is modified when $|x| < 1/\kappa$ to remove the singularity at $x = 0$.

Common to most QLES approaches is the need to perform the decomposition in Equation (1). A widely used approach is to use 1-sparse Hermitian matrices for each U_j . [29] gives quantum circuits for implementing 1-sparse matrices with integer and real coefficients. [30] gives an automatic algorithm for decomposing a d -sparse matrix, H , into a set of 1-sparse matrices by representing H as a graph G_H and colouring the edges of G_H so that no two edges of a vertex share the the same colour. [30] also derived $m = 6d^2$ as the upper bound for the number of 1-sparse matrices in the decomposition. [31] used a 1-dimensional colouring scheme to decompose a tri-diagonal Toeplitz matrix into three 1-sparse matrices with non-integer coefficients. This led to a circuit using phase and X-rotation gates with angles parameterised by the constants in the Toeplitz matrix. [11] performed a direct decomposition of their 2-sparse bi-diagonal matrix for the wave equation into two 1-sparse diagonal matrices. Similarly, [32] who performed resource estimates for a 12, 885² Finite Element mesh with 332,020,680 edges, exploited the banded structure of their FE matrix to decompose the matrix into nine banded 1-sparse matrices. The regular mesh and the FE discretisation made this essentially a Toeplitz matrix with constants along each of the nine diagonals. [33] and [34] developed a *star* decomposition in which each U_j is a *galaxy* with a maximum number $m = 6d$ of galaxies. This traded a decomposition with fewer terms for one in which the U_j matrices were no longer 1-sparse.

A characteristic of previous work is that the decompositions involved matrices with a small number of real valued degrees of freedom. The 8×8 Toeplitz matrix studied by [17] needed only two real numbers to define all the non-zero entries. In this work, more realistic matrices are considered where every non-zero entry in the matrix is assumed to have a unique value. One question this work seeks to answer is, how efficiently can a CFD matrix be decomposed into a linear combination of unitaries? A simulated hybrid CFD solver has been developed based on the well established SIMPLE algorithm [35] and using the HHL algorithm for the QLES. Typical of many CFD solvers is the fact that while the matrix entries change during each non-linear update, the matrix retains a fixed sparsity pattern. A new method is presented for optimising the time taken to re-evaluate the coefficients in the unitary decomposition each time the CFD matrix is updated. The method uses clusters of Pauli strings that have a shared sparsity pattern and has some resonances with the galaxy concept used by [34] although the methodologies used to construct the clusters/galaxies are quite different. The performance of the classical decomposition step is studied for the lid driven cavity test case [36, 37] using CFD meshes ranging from 5×5 nodes to 65×65 nodes. For the two smallest meshes, complete hybrid CFD solution are performed to enable trade studies of the effect of approximating the unitary decomposition on convergence rates. The number of ancilla rotations in the eigenvalue inversion circuit is also studied. In this work, HHL returns the full state vector to the classical solver. This allows the effect of the eigenvalue precision to be studied relative to the

exact solution. Future work will consider the effect of returning a sampled state based on multiple observations, and on approximations in loading the input state.

This work is presented as follows. Section 2 gives an overview of the current state of classical CFD algorithms and considers routes to quantum advantage. This is supplemented by Appendix A which gives a high level overview of the SIMPLE CFD algorithm for readers with little prior knowledge of CFD. Section 3 describes the test case used in this study and gives key parameters for the matrices to be solved. Section 4 describes the emulated hybrid solver framework. This is supplemented by Appendix B which gives the method for efficient unitary decomposition and coefficient re-evaluation. Section 5 presents timing results for the unitary decomposition relative to the classical time for the CFD solver. This is relevant as the decomposition takes place on the classical side of the hybrid interface. Hybrid HHL solutions are also presented and the impact of ignoring unitaries with small coefficients is analysed. Finally Section 6 draws conclusions and the directions for future developments are highlighted.

2 CFD algorithms

Modern CFD codes are highly sophisticated and are able to run reliably on many millions of mesh nodes. [38] used steady CFD calculations with up to 180 million nodes to model the aerodynamic impact of variations in the manufacture of bypass guide vanes in a gas turbine engine. Unsteady CFD has much higher mesh requirements due to the need to resolve the relative motion of adjacent components and features such as shocks and wakes as they propagate through the solution domain. [5] has demonstrated a 5.3 billion node unsteady solution of a compressor using 10,240 cores of the TU Dresden supercomputer, see Figure 1. There are many well established techniques for the hybridisation of classical CFD codes with many able, for example, to mix shared and distributed memory, and vectorization paradigms in a single code base. [39] demonstrate how abstraction layers allow CFD codes to easily run in mixed mode and also to run across hybrid platforms such as CPUs with GPU accelerators.

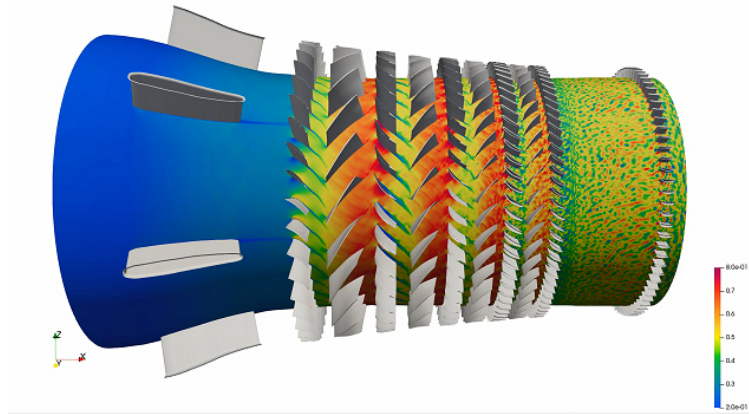


Figure 1: Snapshot from 5.3 billion node unsteady CFD solution from [5].

Whilst the power of quantum computers is expected to advance rapidly, current devices are broadly equivalent to the classical devices of the 1970s in terms of the CFD algorithms and models they can process. At the heart of almost all CFD solvers is a linear equation solver. Although progress is being made on NISQ based CFD solvers [14, 16], quantum CFD solvers that can rival the classical applications described in the previous paragraph will require fault tolerant devices.

The flow of a fluid is governed by the Navier-Stokes equations which express the conservation of mass, momentum and energy:

$$\frac{\partial \rho}{\partial t} + \nabla \cdot (\rho \mathbf{u}) = 0 \quad (2)$$

$$\rho \frac{\partial \mathbf{u}}{\partial t} + \nabla \cdot (\rho \mathbf{u} \otimes \mathbf{u}) = -\nabla p + \mu \nabla^2 \mathbf{u} \quad (3)$$

Where ρ is the fluid density, \mathbf{u} is the fluid velocity, p is the fluid pressure and μ is the dynamic viscosity. Some terms have been dropped from Equations (2) to (3) and the energy conservation equation has been omitted since this paper considers only incompressible, laminar flow.

To solve the Navier-Stokes equations, the SIMPLE (Semi-Implicit Method for Pressure Linked Equations) algorithm of [35] is adopted. This uses *staggered* variables on a 2-dimensional Cartesian lattice. The derivation and implementation of the SIMPLE algorithm are described in Appendix A.

2.1 Considerations for Quantum Advantage

From the description of the SIMPLE algorithm in Appendix A, it may not be apparent that the momentum and pressure correction equations have a different character. The convective nature of the momentum equations means they are *hyperbolic*. Whereas, the pressure correction equations are *elliptic*. The latter require much more computational effort to solve. For example, the pressure correction solution shown in Figure 5a required 11,849 Gauss-Seidel iterations for the pressure correction equation compared to 33 and 36 iterations respectively for the u and v momentum equations. Whilst Gauss-Seidel is a very rudimentary scheme, and modern CFD codes use far more sophisticated solvers, these counts are indicative of the fact that the solution time in modern codes is dominated by the pressure correction equation. Hence the opportunities for quantum advantage are much higher for the pressure correction equation, particularly for very large scale simulations where parallelisation across multiple nodes of a classical supercomputer often results in a block-wise elliptic approach.

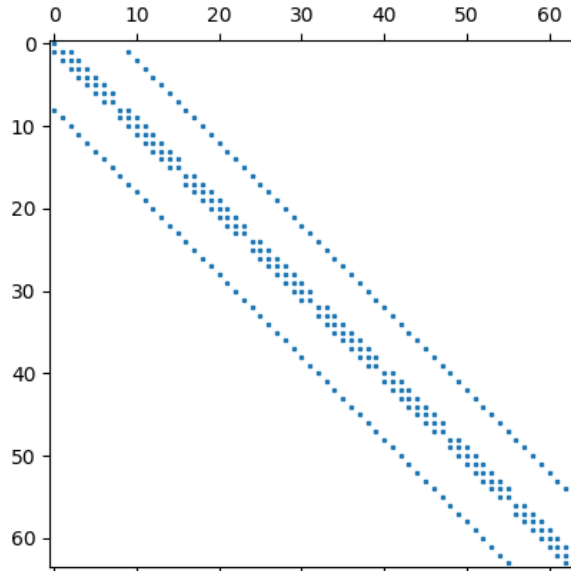


Figure 2: Sparsity pattern of the 8x8 pressure correction matrix for the test case described in Section 3.

Solving an inner linearised matrix or set of matrices is the standard approach used in CFD. This gives a clear opportunity for hybrid calculations where the linearisation of the non-linear Navier-Stokes equations occurs on the classical computer and the resulting linear matrix system(s) is solved on the quantum computer. This work focuses on the hybrid interface and particularly the decomposition of the CFD matrices into a form suitable for a quantum computer. The approach adopted exploits the fact that there may be a large number of outer non-linear iterations and, whilst the matrix entries are updated, the sparsity pattern does not change. A typical sparsity pattern for the pressure correction matrix (A^p in Equation (23)) on a 2D lattice mesh is shown in Figure 2.

3 Test case - lid driven cavity

The lid driven cavity is one of the canonical test cases for CFD with the first published applications dating from the 1970s [36, 37]. This case continues to be used as a basic validation case for viscous incompressible flow solvers on coarse meshes [40].

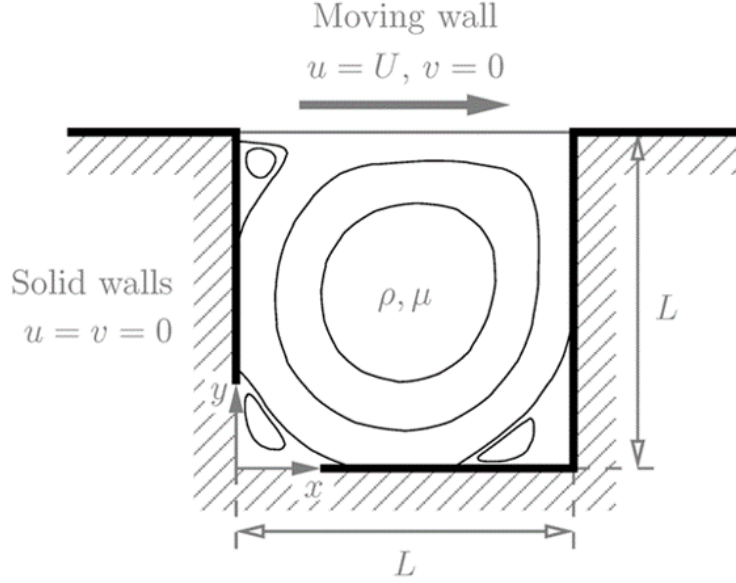


Figure 3: Overview of lid driven cavity test case, from [40].

Whilst, this work considers only low Reynolds number laminar flow, at higher Reynolds numbers this test case exhibits more complicated phenomena such as recirculations, turbulent flow structures and laminar to turbulent transition. Figure 3 from [40] gives an indication of some of the 2 dimensional flow structures. In 3D, the flow demonstrates complex unsteady turbulence phenomena such as inhomogeneous turbulence and small scale helical structures [41, 42]. [42] used a staggered mesh and a derivative of the SIMPLE scheme on a $64 \times 64 \times 64$ mesh. [43] used the equivalent of a $129 \times 129 \times 129$ mesh to perform direct numerical simulations of the turbulent flow in a 3D cavity. Calculations of this type are attractive for quantum computing as they explicitly resolve all the turbulence phenomena and do not require complicated physical models of turbulence. However, this paper considers the 2D cavity with mesh sizes that are likely to be tractable on the first generation of fault tolerant devices.

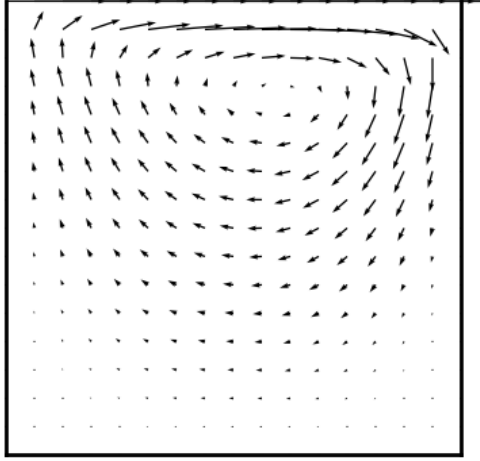
CFD mesh	PC matrix	#non-zeros	sparsity	λ_{min}	λ_{max}	κ	HHL
5x5	16x16	64	25.0%	5.2×10^{-2}	4.54	87.7	15
9x9	64x64	288	7.03%	2.7×10^{-3}	1.51	5.7×10^2	19
17x17	256x256	1,216	1.86%	1.4×10^{-4}	0.49	3.5×10^3	24
33x33	1,024x1,024	4,992	0.48%	7.3×10^{-6}	0.13	1.8×10^4	29
65x65	4,096x4,096	20,224	0.12%	3.8×10^{-7}	0.034	8.9×10^4	33

Table 1: Dimensions, sparsity, eigenvalue range and condition number for pressure correction equations. The HHL column gives an estimate of the number of logical qubits needed by HHL.

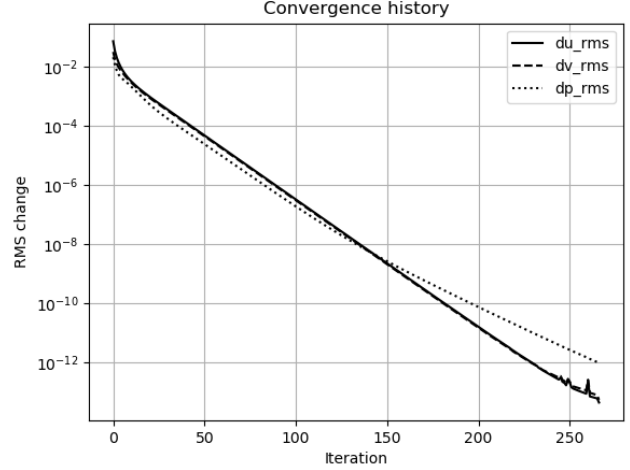
Table 1 lists the mesh dimensions, based on the (x, y) coordinate mesh, used in this study. Also included are the dimensions of the pressure correction matrices and their sparsity as a percentage of the number of non-zero entries relative to a fully populated matrix. Table 1 also includes the minimum and maximum eigenvalues and the condition number, κ for each matrix, computed using the GNU scientific library [44]. For each mesh, the eigenvalues are taken from the pressure correction equation after 10 outer iterations. The table also gives an estimate of the number of logical qubits needed by HHL based on the minimum and maximum eigenvalues. The time taken to compute these is not included in the analysis.

Figure 4a show the velocity vectors from the converged CFD solution on the 17x17 mesh. Figure 4b shows the convergence histories for the momentum and pressure correction equations as the root mean square (RMS) of the updates to each equation. The calculation is performed using double precision arithmetic and the iterations are deemed converged when the RMS updates are all below 10^{-12} .

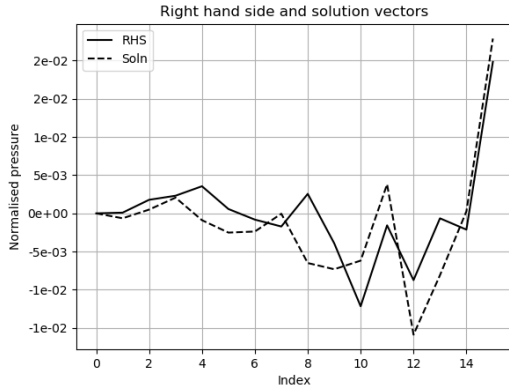
The initial analysis will consider pressure correction matrices sampled from the classical CFD solver after 10 and 100 outer iterations. HHL solutions will be compared with the classical solutions. Figure 5a shows the right hand side input



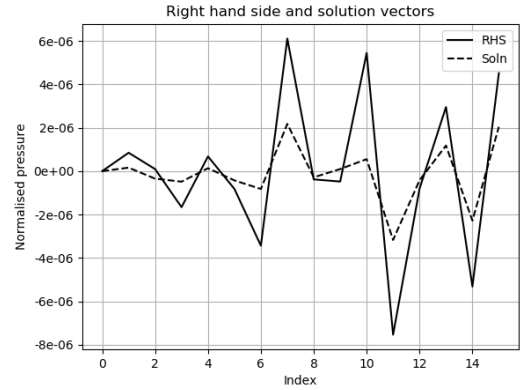
(a) Converged velocity vectors.



(b) Convergence history.

Figure 4: Lid driven cavity: solution and convergence history for 17×17 mesh

(a) 10 iterations.



(b) 100 iterations.

Figure 5: Lid driven cavity: right-hand side and solution vectors of the pressure correction equation after 10 and 100 iterations on the 5×5 mesh.

vector and the solution vector for the the pressure correction matrix after 10 iterations from the 5×5 mesh. Figure 5b shows the same vectors for the matrix after 100 iterations. Similar matrices and vectors for all the meshes listed in Table 1 are available on request.

4 Hybrid CFD solver

Figure 6 gives an overview of the hybrid CFD solver whereby the time consuming pressure correction equation would be solved on a quantum device. In this work, the Quantum Linear Equation Solver (QLES) is emulated on a classical device.

4.1 Matrix preparation

In order to process the CFD matrix on a quantum device it must be decomposed into a linear combination of unitaries (LCU). The fixed sparsity pattern of the pressure correction matrix means that the same set of unitaries can be used throughout the hybrid solver with only the LCU coefficients updated each time the hybrid interface is called.

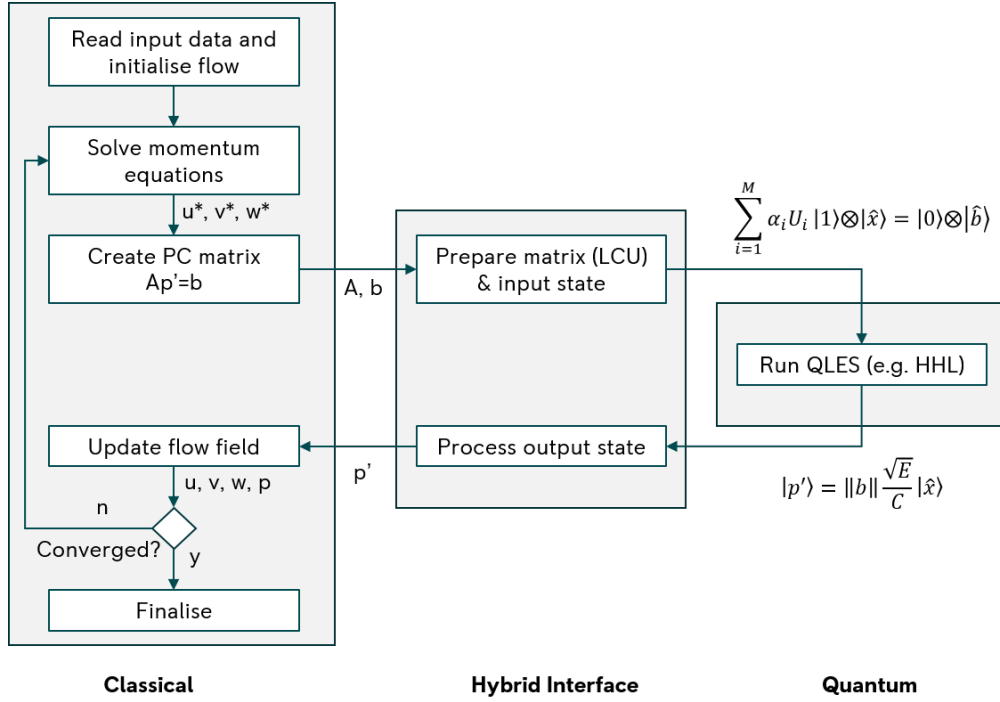


Figure 6: Hybrid CFD solver for the SIMPLE algorithm. Hats denote normalised variables.

The linearised system shown in Figure 6 solves a matrix equation of the form $A|x\rangle = |b\rangle$. As discussed in Appendix B, the matrix A is non-symmetric and in order to create a unitary decomposition it must be *symmetrised* such that:

$$H = \begin{pmatrix} 0 & A \\ A^\dagger & 0 \end{pmatrix} \quad (4)$$

And the linear system to be solved becomes:

$$H \begin{pmatrix} 0 \\ x \end{pmatrix} = \begin{pmatrix} b \\ 0 \end{pmatrix}$$

The task for the classical part of the hybrid solver is to express H as a linear combination of M unitaries:

$$H = \sum_{i=1}^M \alpha_i U_i \quad (5)$$

In this work, a new approach based on the orthogonality of grand sums of Hadamard products of Pauli strings is used. This is described in full in Appendix B.3 which also describes other LCU approaches including those based on the trace orthogonality of products of Pauli matrices, commonly termed Pauli strings.

Table 2 compares the times for the initial LCU decomposition and for the re-evaluation of the coefficients using the trace and Hadamard orthogonality approaches. For validation, both approaches produce an identical number of unitaries in each decomposition. For the Hadamard based approach, the numbers in brackets indicate the number of clusters that were found. Both decompositions are compared with the original matrix to confirm that they are equivalent. In all cases the L_2 norm of the differences between the original and the unitary decomposition are $\mathcal{O}(10^{-15})$.

Comparing the execution times, Table 2 shows significant benefits for the Hadamard approach for both the initial decomposition and the coefficient re-evaluation. Even on a modest 512×512 matrix, the trace orthogonality approach is 30 times slower for the initial decomposition and 10 times slower for the coefficient re-evaluation. On the 2048×2048 matrix, the trace approach is estimated to require 17 hours based on the time to complete 10% of the trace orthogonality checks. This is nearly 600 times slower than the Hadamard approach. Since the trace based decomposition did not run to completion, the coefficient evaluation time could not be evaluated.

Dimensions H Matrix (sparsity)	Trace orthogonality			Hadamard orthogonality		
	#unitaries	decomp time	coeff time	#unitaries	decomp time	coeff time
32x32 (12.5%)	63	0.0104	0.00024	63 (5)	0.006	0.0001
128x128 (3.51%)	319	0.8882	0.0156	319 (7)	0.047	0.0016
512x512 (0.93%)	1535	106.1	0.592	1,535 (9)	3.211	0.0548
2,048x2,048 (0.24%)	-	63,375*	-	7,167 (11)	111.4	0.9423
8,192x8,192 (0.06%)	-	-	-	32,767 (13)	6,713	17.76

Table 2: Comparison of decomposition and coefficient re-evaluation times of the matrices in Table 1. Hadamard unitaries column includes #clusters in brackets. All times in seconds. * Estimate based on time to complete 10% of products.

The Hadamard approach creates clusters which include all Pauli strings that share the cluster’s sparsity pattern. Some clusters contain products that always have zero coefficients. For example, for the 512×512 matrix, the 9 clusters contain a total of 2,304 Pauli strings of which 769 always have a zero coefficient. The processing of these is included in the timings in Table 2 although only those unitaries with a non-zero coefficient are included in the number of unitaries. The zero coefficients arise because, whilst the PC matrix is non-symmetric, it does have a large number of symmetric entries due to the finite volume discretisation that has been used.

Although the Hadamard approach has less severe scaling than the trace approach, it took almost 2 hours to complete the LCU for the $8,192 \times 8,192$ matrix. This corresponds to a 65×65 CFD mesh which is the level needed to investigate turbulence phenomena. This is a mesh of 4,225 nodes which is several orders of magnitude below the meshes discussed at the start of Section 2; and, far below the 166 million element mesh at which [32] estimated quantum advantage would be achieved. Although the LCU decomposition can be efficiently parallelised, it is likely to remain a significant bottleneck in hybrid CFD algorithms.

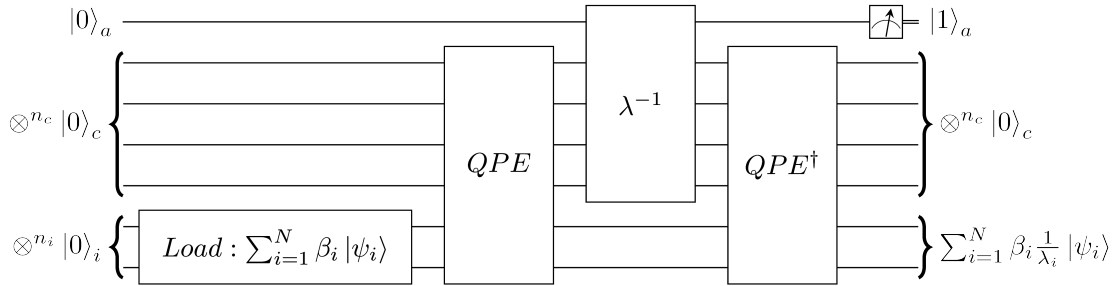


Figure 7: Outline of HHL algorithm [13].

4.2 Matrix solution

The focus of this analysis is to demonstrate how the methodology shown in Figure 6 can be used to investigate the classical-quantum interface in a hybrid CFD solver. For this, a completely error free quantum computer is emulated with a full state loader as the input to HHL [13] and the full state vector as output from HHL. Whilst this level of state preparation and measurement (SPAM) cannot be achieved in practice it does allow some of the circuit parameters to be investigated.

The HHL algorithm [13] has been widely reported elsewhere and is not repeated here. The implementation details of the state vector simulator are:

- **State preparation.** In emulation mode, it is enough to directly write the input vector into the amplitudes of the state vector. However, this is not a framework for future study. Instead, the binary tree loader reported as algorithm 1 by [45] is used. This creates a sequence of controlled one-qubit $N - 1$ rotations for an input vector of rank N . [46].
- **Matrix preparation.** The linear combination of unitaries are created using the procedure described in Appendix B.3. The exponentiation of the sum of unitaries is approximated using the Trotter product formula [47]. This creates a single unitary U to be used in the phase estimation step.

- **Phase Estimation.** The powers of U applied to the input register are computed using a simple recursion: $U^{2^n} \leftarrow U^n U^n$. No circuit considerations are taken into account when emulating the phase estimation step or the previous Trotterisation step.
- **Eigenvalue Inversion.** The Polynomial State Preparation (PSP) of [31, 17] is used for the simulated eigenvalue inversion circuit. The inversion function $\sin^{-1}\left(\frac{1}{x}\right)$ is directly computed rather than estimated by a truncated Taylor series polynomial.
- **Ancilla measurement.** For simulation, the ancilla qubit is directly projected onto the $|1\rangle$ state. Since the simulation has full access to the state vector, the expectation, E , of the $|1\rangle$ state being measured can be directly computed.
- **Dimensional state vector.** The normalised solution, $|\hat{x}\rangle$, generated by HHL is re-dimensionalised by:

$$|x\rangle = \|b\| \frac{\sqrt{E}}{C} |\hat{x}\rangle \quad (6)$$

Whilst E is directly accessible in a simulation, it is a measured quantity on a physical device. Although it has not been tested in this work, marginal probabilities derived from the state vector allow rapid emulation of a very large number of physical measurements, albeit within the limits of classical pseudo random number generators. Accurate re-dimensionalisation of the measured quantum state is expected to be an important factor in hybrid CFD algorithms.

As shown in Figure 6, the full (simulated) state vector is returned to the hybrid interface.

5 Results

All results were run on a desktop PC with an Intel® Core® i9 12900K 3.2GHz Alder Lake processor and 64GB of DDR4 RAM. All calculations were run in serial mode. Whilst serial execution may affect the precise performance results, the relative comparisons between the unitary decomposition and the CFD solver run times are broadly valid. However, the timings should only be taken as indicative as only preliminary code optimisation has been performed for both the CFD solver and the hybrid interface. All performance comparisons exclude the time taken to simulate HHL.

In all tests, the matrices created by summing the unitaries were compared with the original CFD matrices and, in all cases, the differences were $\mathcal{O}(10^{-15})$ or less and, therefore, within the rounding error of the double precision arithmetic used in the algorithm. This section first analyses the unitary decompositions that are produced. The decompositions are then used as the basis for simulated HHL solutions. Firstly, the individual pressure correction matrices sampled from the classical CFD run are considered. Secondly, a full hybrid run of the CFD solver is performed with each pressure correction step being solved using the unitary coefficient update procedure and the HHL algorithm.

CFD mesh	#unitaries	% non-zeros	decomp time	coeff time	CFD time	Hybrid O/H
5x5	63	50.0%	0.006	0.0001	0.0085	4.8
9x9	319	55.6%	0.047	0.0016	0.056	8.1
17x17	1,535	62.7%	3.211	0.0548	1.127	15.0
33x33	7,167	71.8%	111.4	0.9423	12.13	28.6
65x65	32,767	81.0%	6,713	17.76	210.1	53.1

Table 3: Comparison of decomposition and coefficient re-evaluation times for the matrices in Table 1 including comparison with the CFD solver time. All times in seconds.

5.1 Unitary decomposition and coefficient update

Table 3 shows the unitary decomposition times for the range of CFD meshes using the pressure correction equation after 10 outer iterations. The corresponding eigenvalues and condition numbers were given in Table 1. The number of unitaries as a percentage of the number of non-zeros in the matrix shows that the number of unitaries is rising slightly faster than $\mathcal{O}(N)$. The unitary decomposition times from Table 2 are compared with the time taken for a complete classical CFD solution. On all meshes, the one-off initial unitary decomposition time is roughly equal to or much greater than the time for the classical CFD solution. The column labelled 'Hybrid O/H' is the accumulated time of the unitary decomposition (one-off and repeated coefficient evaluations) divided by the time to run the CFD solver. This roughly doubles each time the mesh size increases to the point that the time spent in the hybrid interface on the

65x65 mesh is 53 times that of a classical CFD solution. All the timings are purely for those hybrid tasks that must be performed on a classical computer and exclude the time to emulate HHL.

Considering the finite element mesh of [32] with 332,020,680 edges, each edge corresponds to 2 entries in the assembled matrix. The scaling of Table 3 suggests that the corresponding LCU would consist of the order of one billion unitaries if this were a CFD mesh.

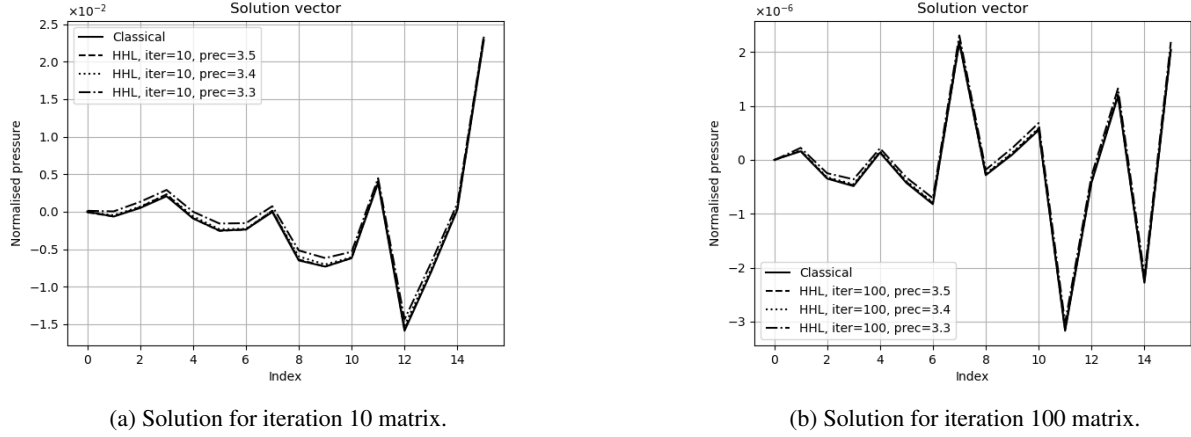


Figure 8: HHL solutions for the 5×5 mesh saved after 10 and 100 outer iterations. The precision $m.n$ indicates m integer qubits and n fraction qubits. All cases have a sign qubit, meaning the clock register contains $m + n + 1$ qubits.

5.2 HHL solutions for sampled pressure correction matrices

Figure 8 compares the HHL solutions for the iteration 10 and 100 pressure correction matrices and input vectors shown in Figure 5. For the HHL solutions, three precision settings are considered for the QPE clock register. Since the symmetrised matrix, H , has negative eigenvalues, all calculations require a sign qubit. The precisions considered give the following ranges and numbers of qubits:

- 3.3 - range $[\pm 0.125, \pm 8.875]$ using 7 clock qubits and 13 qubits in total.
- 3.4 - range $[\pm 0.0625, \pm 8.9375]$ using 8 clock qubits and 14 qubits in total.
- 3.5 - range $[\pm 0.03125, \pm 8.96875]$ using 9 clock qubits and 15 qubits in total.

The total number of qubits includes 5 for the input register and 1 for the ancilla qubit. Comparing with the eigenvalues from Table 1 it can be seen that all precisions cover the largest eigenvalue of 4.54, but only the last one covers the lowest eigenvalue of 5.2×10^{-2} .

Figure 8a shows that best precision (3.5) matches almost exactly the classical solution. The 3.4 precision HHL solution is also very close to the the classical solution. At the 3.3 precision, the HHL solution is starting to degrade. Figure 8b shows that the simulated HHL performs well even for input states with a norm close to the single precision limit for real numbers. Table 4 shows the influence of the precision on the fidelity between the HHL and exact solutions. Of interest is the fact that the fidelity does not degrade as the magnitude of the input vector reduces between 10 and 100 iterations. However, the expectation of the ancilla qubit being in the $|1\rangle$ state does reduce from 0.6% to 0.05%.

Precision	10 iterations	100 iterations
3.3	0.99342	0.99593
3.4	0.99934	0.99963
3.5	0.99977	0.99991

Table 4: Fidelity between HHL solution and exact solution on sample matrices for 5×5 mesh.

Based on these results, the 3.4 precision option is used for the subsequent simulations on the 5×5 mesh.

5.3 Hybrid HHL solutions for cavity test case

Figure 9 compares the convergence histories of the classical and hybrid solutions with both terminated after 250 outer iterations for the 5×5 CFD mesh. The graphs show the two measures of convergence of the pressure correction equation: the root mean square of the pressure correction and the root mean square mass conservation residual. The convergence histories for the u and v velocities have the same character as the pressure correction convergence.

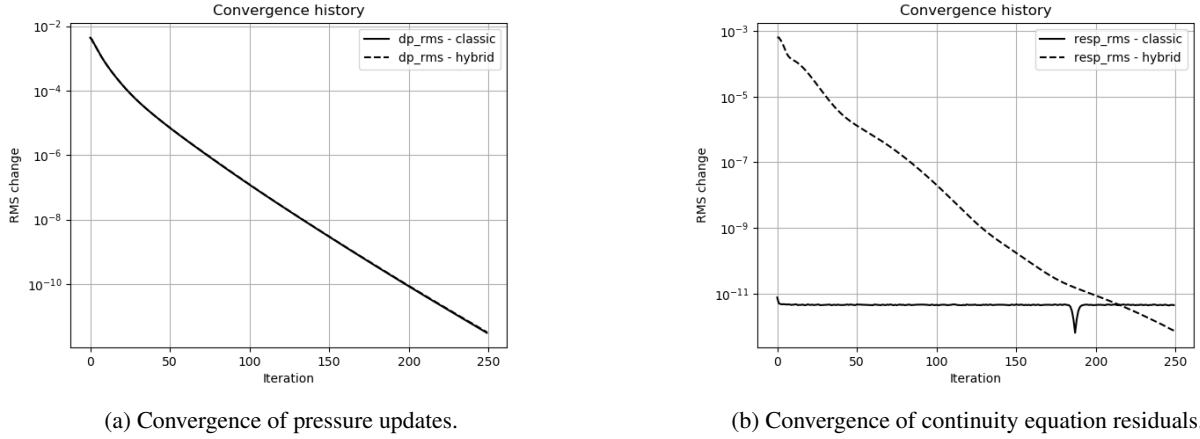


Figure 9: Comparison of classical and hybrid convergence histories for 5×5 mesh.

For the convergence of the pressure correction update, Figure 9a, the classical and hybrid schemes are essentially identical. More interesting is the convergence of the mass conservation residual in Figure 9b. A feature of the SIMPLE scheme is that the pressure correction equation is linear and, hence, the corrected velocities should satisfy the continuity equation to within machine precision. The classical solution achieves this. The hybrid solution does not, which indicates that some of the finer details of the pressure correction solution are lost due to the precision of the clock register. Nevertheless, the hybrid scheme is able to converge the continuity residual to close to machine precision by the 250th iteration. The reason that an HHL precision of 3.4 can achieve a residual precision of $\mathcal{O}(10^{-12})$ is the normalisation of the input vector. The differences in the continuity residual do not affect the momentum equations for which the match between the classical and hybrid solutions is the same as for the pressure corrections. These results were somewhat unexpected as it was anticipated that the reduced precision of the HHL clock register would have a larger impact.

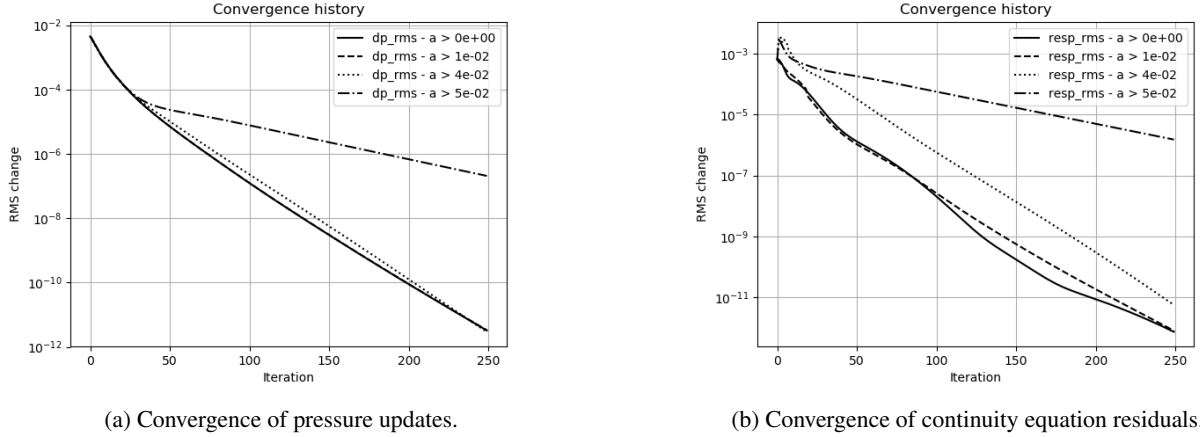
5.3.1 Partial unitary decompositions

To illustrate the use of a simulated hybrid framework, the influence of ignoring unitaries in the LCU that have small coefficients is considered. Table 5 shows the impact of increasing this threshold on the number of unitaries in the LCU using the sampled pressure correction matrix after 10 outer iterations. The limits were chosen heuristically based on roughly halving the number of unitaries for $|\alpha| > 4 \times 10^{-02}$ and halving again for $|\alpha| > 5 \times 10^{-02}$.

LCU coefficient limit	number of unitaries
1×10^{-06}	63
1×10^{-02}	53
2×10^{-02}	48
3×10^{-02}	46
4×10^{-02}	33
5×10^{-02}	14
1×10^{-01}	10

Table 5: Influence of ignoring small coefficients on number of unitaries in LCU, sample pressure correction matrix after 10 iterations. Coefficients with $|\alpha|$ less than the limit are ignored.

Figure 10 shows the influence of ignoring small LCD coefficients on the convergence of the hybrid CFD solver. If the limit is set to 1×10^{-02} approximately 15% of the coefficients are ignored and, other than small impact on the continuity residual, the impact is negligible. Increasing the limit to 4×10^{-02} omits just under 50% of the coefficients



(a) Convergence of pressure updates.

(b) Convergence of continuity equation residuals.

Figure 10: Influence of ignoring small LCD coefficients on convergence of the hybrid CFD solver.

and whilst the impact is more noticeable, the rate of convergence is only marginally impacted. Increasing the limit further to 5×10^{-02} now omits over 75% of the coefficients and markedly degrades the rate of convergence. However, the results for the 5×10^{-02} limit do suggest that the calculation would eventually converge. As is often observed in CFD, the boundary between good and poor behaviour is quite narrow and thresholds are usually case dependent. An approach based on omitting the 50% of unitaries that have the lowest coefficients may enhance the performance of the quantum circuit but does not help the hybrid interface as this is an iteration by iteration assessment that requires the full unitary decomposition.

5.3.2 Eigenvalue inversion

The reason that Table 4 shows such high fidelities for the HHL solutions is that the eigenvalue inversion circuit has used a full bit-wise accurate circuit. In the terminology of [31], the eigenvalue inversion circuit as the same degree has the number of clock qubits.

Figure 11 illustrates such a full degree inversion for a circuit with 4 clock qubits. As can be seen, all possible bit patterns are used to control separate rotations of the ancilla qubit. This leads to an inversion circuit of depth $2^{n_c} - 1$. For larger clock registers, the simulation time is dominated by the eigenvalue inversion. Since this is an $\mathcal{O}(N)$ circuit it is also likely to scale poorly on physical devices. It is, therefore, instructive to consider the accuracy of the eigenvalue inversion circuit on the CFD solution.

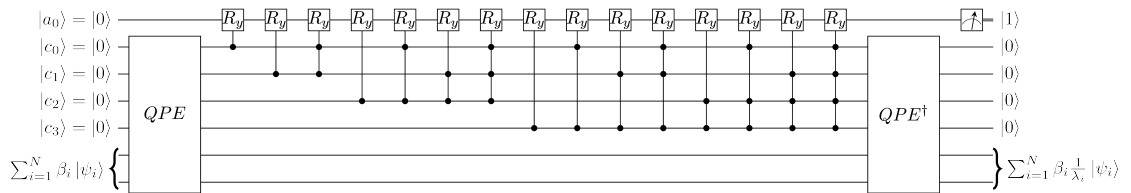


Figure 11: Sample HHL circuit with full degree eigenvalue inversion circuit.

One of the rationales of polynomial state preparation [31] is that smooth functions can be approximated by low degree polynomials and hence shallower circuits. However, the state of the clock register after QPE is likely to be highly non smooth with peaks corresponding to the eigenvalues and troughs elsewhere. With a precision of ± 3.4 for the 5×5 mesh, the full eigenvalue inversion circuit is of order 8 and contains 255 ancilla rotations giving a fidelity of 0.99963 from Table 4. Reducing the order to 7, saves just one rotation and reduces the fidelity to 0.98841. Reducing the order to 6, saves 9 rotations and reduces the fidelity to 0.88418. As expected, reducing the order of the circuit strongly affects the solution and saves hardly any rotations.

An alternative is omit those bit-patterns in the PSP that have a low probability after phase estimation. This is easy to implement in a simulation but would be hard on a physical device. After QPE the state space amplitudes contain the probabilities that each bit-pattern in the clock register corresponds to an eigenvalue, although these are embedded with

the state-space amplitudes for the entire circuit. In emulation, marginal probabilities for the clock register can be easily extracted from the state space amplitudes. These can be used to omit the ancilla rotations for states that have a small marginal probability.

Table 6 shows the effect of the probability limit on the number of ancilla rotations and the fidelity for the 5×5 sample matrix after 10 and 100 outer iterations. At 10 iterations, a limit of 1×10^{-04} has a marginal effect on the fidelity and over half the ancilla rotations are saved. At 100 iterations, a larger number of ancilla are saved and even at a limit of 1×10^{-03} a fidelity greater than 0.99 is achieved.

Probability Limit	10 iterations		100 iterations	
	No. of ancilla rotations	Fidelity	No. of ancilla rotations	Fidelity
1×10^{-06}	255	0.99593	255	0.99963
1×10^{-05}	192	0.99336	156	0.99963
1×10^{-04}	120	0.99278	80	0.99489
1×10^{-03}	68	0.98574	36	0.99426

Table 6: Influence of omitting ancilla rotations below the marginal probability limits on the sample matrix after 10 and 100 iterations for 5×5 mesh.

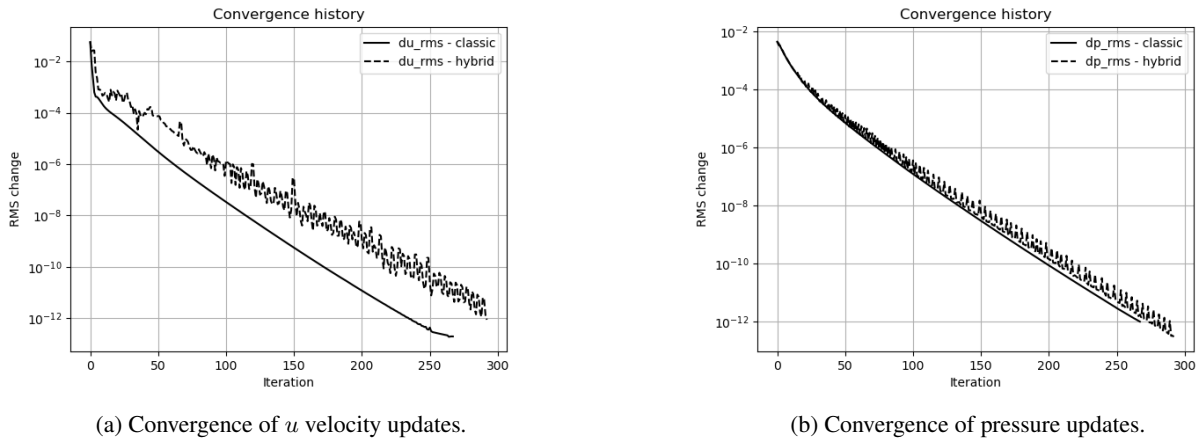


Figure 12: Convergence histories on 5×5 mesh for eigenvalue inversion where ancilla rotations with a marginal probability $< 1 \times 10^{-03}$ are ignored.

Figure 12 shows the u -velocity and pressure convergence histories where ancilla rotations with a marginal probability $< 1 \times 10^{-03}$ are ignored. Whilst the fidelities in Table 6 suggest this limit should have a marginal effect, there is a noticeable impact on convergence of the u -velocity. The convergence also demonstrates a more oscillatory nature which is characteristic of integer decisions (the number of rotations to ignore) which are based on real-valued thresholds (the marginal probability). However, the hybrid solution does still converge after 293 outer iterations compared to 268 for the classical solver. As in classical computing a scheme that requires more rapid iterations may out-perform a scheme that user fewer more complicated iterations. Unfortunately, this assessment can only be performed with a meaningful outcome on a physical device.

5.4 9x9 mesh

Results for the 9×9 mesh are briefly considered in this section. The precision required to span the eigenvalue range shown in Table 1 is ± 1.9 . The smallest non-zero number that can be represented by this precision is 1.95×10^{-03} which compares to the smallest eigenvalue from Table 1 of 2.7×10^{-03} . Table 7 combines the effects of precision and marginal probability for the pressure correction matrix after 10 iterations for the 9×9 mesh. As expected, it is only with a precision of ± 1.9 that a fidelity > 0.99 is reached. However, reducing the number of fraction qubits has a more marked effect than for the 5×5 case shown in Table 4. In the 5×5 case, a 2 qubit reduction still produces a fidelity > 0.99 whereas for the 9×9 case the fidelity drops to < 0.95 . This is first indication that results for small meshes may not extrapolate to larger ones.

Precision	Full circuit		Partial circuit	
	No. of ancilla rotations	Fidelity	No. of ancilla rotations	Fidelity
1.6	511	0.93846	511	0.93846
1.7	1,023	0.94503	594	0.94503
1.8	2,048	0.98447	616	0.98446
1.9	4,095	0.99967	982	0.99965

Table 7: Influence of precision and omitting ancilla rotations below a marginal probability of 1×10^{-06} on the sample matrix after 10 iterations for the 9×9 mesh.

Figure 13a compares the HHL solutions at the listed precisions with the classical solution for a sampled matrix after 10 iterations from the 9×9 mesh. The classical and ± 1.9 precision solutions are identical as expected from the fidelity in Table 6. The lower precisions show the same character as the classical solution but are offset and in some of the smaller values have the opposite sign. The ± 1.6 solution is omitted as it is very close to the ± 1.7 solution.

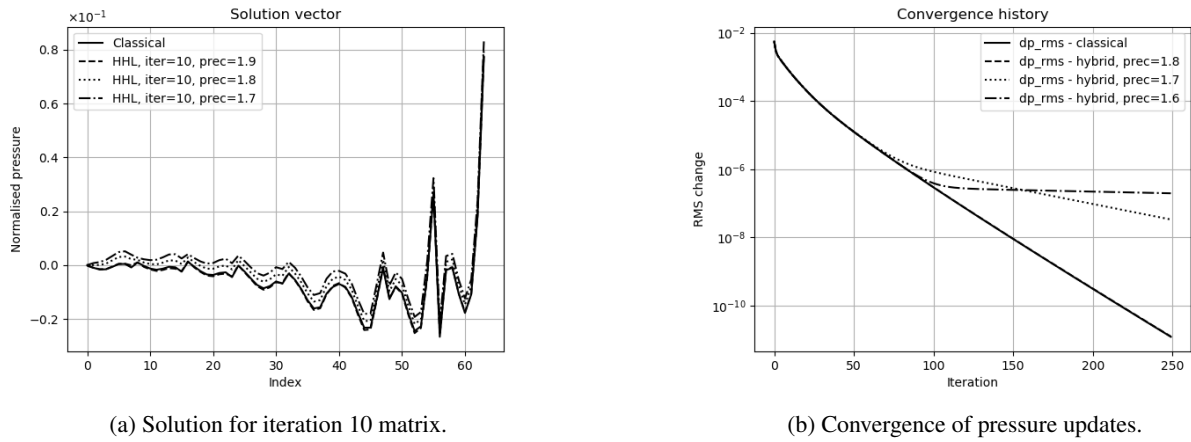


Figure 13: Comparison of classical and HHL solutions for the 9×9 mesh matrix after 10 iterations; and, the full CFD solution using HHL with precision ± 2.6 for 100 iterations.

Figure 13b compares the full CFD convergence history for the classical and hybrid solutions. The ± 1.9 precision hybrid case was not run as the ± 1.8 precision solution is virtually identical to the classical solution. The impact of the drop in fidelity in Table 7 is seen in the convergence histories for the ± 1.6 and ± 1.7 solutions. The latter does appear as though it would ultimately converge, but the ± 1.6 convergence has stagnated. In general, the larger eigenvalues, which are all retained, correspond to the larger scale flow structures. The smaller eigenvalues correspond to structures that vary between mesh cells. Omitting these appears to prevent the cell-wise residuals being reduced to machine precision.

In CFD literature, it is common to express errors in terms of their root mean square (RMS):

$$e_{rms} = \sqrt{\frac{1}{N} \sum_{k=1}^N |\delta x_k|^2} \quad (7)$$

Table 8 lists fidelities and error norms for the solution of the matrix after 10 iterations. This suggests that the RMS error cannot be much above 1% before the hybrid algorithm struggles to converge. This is likely to have implications for the fidelity with which the *pseudo* state vector is reconstructed from measurements on a physical quantum computer.

The foregoing analysis of the results has demonstrated that with fidelities greater than 0.98, a hybrid HHL solution can produce results of equal quality to the classical solution. There are some options for reducing the number of unitaries in the LCU and for reducing the number of rotations of the ancilla qubit in the eigenvalue circuit. It is recognised that the latter would be a challenge to implement on a physical device. In most cases, the reductions have maintained fidelities above or close to 0.99 for the match between the HHL solution and the classical one. Below this, the 9×9 mesh

Precision	Fidelity	L_2 error norm	RMS error
1.6	0.9385	0.3507	0.0310
1.7	0.9450	0.3319	0.0293
1.8	0.9848	0.1721	0.0154
1.9	0.9997	0.0245	0.0022

Table 8: Fidelity and error norms between HHL solution and exact solution on for sample matrix after 10 iterations for the 9×9 mesh.

solutions have shown that the quality of the inner QLES solution affects the convergence of the outer CFD solution. This can be just a reduced rate of convergence or a stagnation of convergence.

6 Conclusions

A concern for future quantum advantage for CFD applications is the computational effort required on the classical side of a hybrid interface. This could lie in classical costs associated with data preparation or circuit design or some other factor yet to emerge. It is certainly not axiomatic that the computational cost of the hybrid interface will be lower than the cost of performing the equivalent classical CFD calculation; or, that making it so does not incur significant classical supercomputing costs.

An emulation of a hybrid CFD solver using HHL on the smallest 5×5 mesh has produced benchmark results showing that HHL does not need full 64-bit precision to match the iterative performance of the CFD solver and can achieve convergence levels of $\mathcal{O}(10^{-12})$. However, preliminary timing results suggest that the classical side of the hybrid interface causes the hybrid solver to take 10 times longer than the classical solver.

An investigation of the number of unitaries in the LCU for CFD matrices up to 65×65 shows that the number of unitaries scales slightly faster than linearly in the number of non-zeros in the CFD matrix, with the largest matrix requiring 32,767 Pauli strings. A new Hadamard based orthogonality approach for finding the Pauli strings in a LCU outperforms the trace orthogonality approach on the test matrices. However, it only marginally delays the inevitable impact of the $> \mathcal{O}(N^2)$ scaling. For the 65×65 , finding the Pauli strings in the LCU decomposition alone takes 30 times longer than the full CFD solver. The Pauli string algorithm is more easily parallelised than a CFD solver but the cross-over point for industrial scale CFD applications is likely to require significant super-computing costs. Note that classical parallelisation does not reduce compute resources, it speeds up execution by amassing the resources of multiple devices.

An analysis based on omitting unitaries with small coefficients has shown that up to half the unitaries can be omitted in the QLES without materially affecting the convergence of the hybrid solver. However, there is a small margin before further omissions degrade the performance. Dynamic algorithms that omit 50% of unitaries with the lowest coefficients would aid the quantum circuit but not the classical costs of the hybrid interface.

A study of the eigenvalue inversion circuit has shown that a full order circuit is needed to match the classical solution. Using the fact that the emulation has full access to the state vector after the QPE step has shown, the unsurprising result, that ancilla rotations for eigenvalues with low probabilities can be ignored. For the 9×9 mesh this corresponded to a saving of over 75%. However, this is not considered a practical alternative for real devices. For the largest 65×65 mesh, the number of clock qubits for QPE is estimated to be 20 giving a full order eigenvalue inversion circuit with 1,048,576 ancilla rotations. It does not seem unreasonable to expect that industrial CFD applications will require clock registers with at least 32 qubits and possibly 64 qubits with the latter requiring a full eigenvalue inversion circuit with $\mathcal{O}(10^{19})$ ancilla rotations.

This paper began by comparing the current state of quantum CFD with that of classical CFD in the 1970s. The intervening years have taught us that performance bottlenecks can be overcome. There are other quantum algorithms for solving linearised equations, most notably Quantum Singular Value Transformation (QSVT). These are equally likely to require classical pre-processing whose compute costs scale with the problem size at faster rate than the quantum solver. In the case of QSVT, these are likely to be the costs of calculating κ and the phase factors for the rotations of the signal qubit. Non-linear quantum CFD algorithms are likely to emerge which will reduce or eliminate the iteration to iteration classical pre-processing, but the effort required by the initial one-off classical pre-processing is unclear and, as shown, this can be dominant. Whatever the algorithm, quantum advantage for industrial scale CFD is very likely to be reliant on classical supercomputing. The question is how much?

Finally, this work has sought to provide CFD test cases and benchmark solutions that can be feasibly run on the first generation of fault tolerant devices.

7 Data availability

The sample matrices and vectors for the meshes listed in Table 1 after 10 and 100 iterations are available from the author upon request.

8 Acknowledgements

The permission of Rolls-Royce to publish this paper is gratefully acknowledged. The HHL results were completed as part of funding received under the UK's Commercialising Quantum Technologies Programme (Grant reference 10004857). This work has benefited from several technical discussions and the author would like to thank Neil Gillespie, Joan Camps and Christoph Sunderhauf of Riverlane; and, Jarrett Smalley of Rolls-Royce.

A The SIMPLE CFD algorithm

The objective of this appendix is to provide sufficient detail of Computational Fluid Dynamics (CFD) to describe the context in which quantum algorithms may be applied. The descriptions are intended to give a high level overview to those with little prior knowledge of CFD. Whilst there are a range of CFD algorithms and modelling choices, attention is restricted to the SIMPLE (Semi-Implicit Method for Pressure Linked Equations) algorithm [35], [37]. Derivatives of this algorithm are still widely used in modern industrial CFD codes, e.g. [48].

To simplify the derivation, consider the steady 2-dimensional form of the Navier-Stokes equations Equations (2) to (3) which can be written in component form as:

$$\begin{aligned} \frac{\partial \rho u}{\partial x} + \frac{\partial \rho v}{\partial y} &= 0 \\ \frac{\partial \rho u u}{\partial x} + \frac{\partial \rho v u}{\partial y} &= -\frac{\partial p}{\partial x} + \frac{\partial}{\partial x} \left(\mu \frac{\partial u}{\partial x} \right) + \frac{\partial}{\partial y} \left(\mu \frac{\partial u}{\partial y} \right) \\ \frac{\partial \rho u v}{\partial x} + \frac{\partial \rho v v}{\partial y} &= -\frac{\partial p}{\partial y} + \frac{\partial}{\partial x} \left(\mu \frac{\partial v}{\partial x} \right) + \frac{\partial}{\partial y} \left(\mu \frac{\partial v}{\partial y} \right) \end{aligned} \quad (8)$$

A.1 Discretisation

Analytical solutions to the Navier-Stokes equations exists in only the rarest cases and practical applications of CFD require a numerical solution procedure. The equations are solved over a region of interest with specified conditions applied at the boundaries of the region.

In order to solve the equations numerically, the continuous flow variables are represented by a discrete set of values, e.g.

$$u_{i,j} \simeq u(x_i, y_j), \quad i = 1, n, \quad j = 1, m \quad (9)$$

where $(x_i, y_j) \in \mathcal{M}_u \subset \mathbb{R}^2$. \mathcal{M}_u is the *mesh* that contains the coordinates of all the points, usually called nodes, at which discrete values of u will be computed. There are two important properties of this structure:

- The mesh coordinates can be referenced independently by indices i and j in the x and y directions. This means that the mesh has a lattice structure. In general, the lattice can be stretched and distorted, as is needed, for example, to model the flow over a curved body such as an airfoil. For this study, a simple Cartesian lattice is sufficient.
- The mesh coordinates for each flow variable do not need to be the same. Here, the *staggered* mesh arrangement of [49] and [35], is used in which there are separate meshes \mathcal{M}_u , \mathcal{M}_v and \mathcal{M}_p for the discrete values of u , v and p . This arrangement is illustrated in Figure 14.

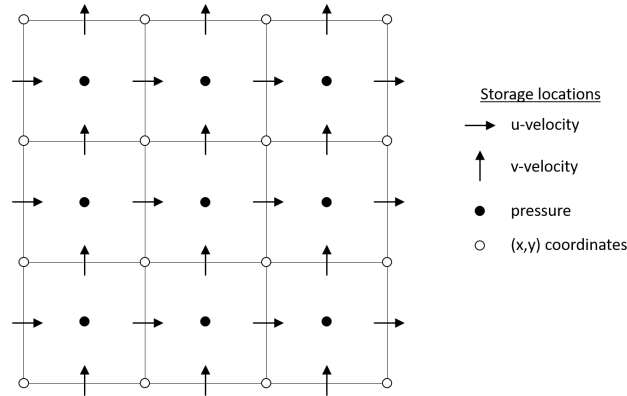


Figure 14: Staggered mesh arrangement for SIMPLE pressure correction solver.

To discretely represent the derivatives in Equation (8), Taylor series expansions are used:

$$u(x + \Delta x, y + \Delta y) = u(x, y) + \Delta x \frac{\partial u}{\partial x} + \Delta y \frac{\partial u}{\partial y} + \mathcal{O}(\Delta x^2, \Delta y^2, \Delta x \Delta y) \quad (10)$$

For Cartesian lattice meshes, this gives:

$$\begin{aligned}\frac{\partial u}{\partial x} &= \frac{u(x+\Delta x, y) - u(x, y)}{\Delta x} + \mathcal{O}(\Delta x) \\ \frac{\partial u}{\partial x} \Big|_{i+\frac{1}{2}, j} &\simeq \frac{u_{i+1, j} - u_{i, j}}{x_{i+1} - x_i}\end{aligned}\quad (11)$$

The number of mesh nodes in the discrete meshes is determined by the user and is driven by the complexity of the geometry being modelled and the solution accuracy required. As Equation (11) shows the smaller the mesh spacing, Δx the more accurate the Taylor series approximation. Hence, a dense mesh with a large number of closely spaced nodes gives a more accurate solution than a coarse mesh with the nodes widely spaced.

Repeating the Taylor series expansions for the other derivatives yields a set of discrete equations in terms of the values of u, v, p at the nodes of their respective meshes, $\mathcal{M}_u, \mathcal{M}_v$ and \mathcal{M}_p . To solve the discrete equations the *finite volume* method is used. Details of the methodology are given in Chapter 6 of [6]. The control volumes for each variable are shown in Figure 15.

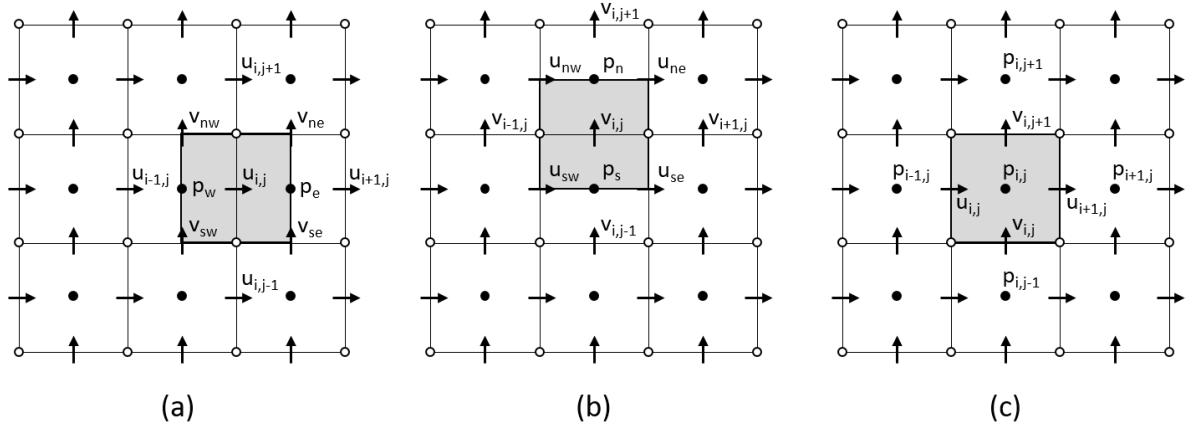


Figure 15: Control volume arrangement for staggered meshes. (a) u -velocity control volume, (b) v -velocity control volume, and (c) pressure control volume.

A.2 Momentum conservation equations

For the u -momentum in Equation (8), integrating over the control volume in Figure 15 and using the divergence theorem gives:

$$\int_{e,w} \rho u u dy + \int_{n,s} \rho v u dx = - \int_{e,w} p dy + \int_{e,w} \mu \frac{\partial u}{\partial x} dy + \int_{n,s} \mu \frac{\partial u}{\partial y} dx \quad (12)$$

Where the integrals labelled e, w are over the east and west sides of the face and those labelled n, s are over the north and west faces. This form is possible due to the Cartesian nature of the control volume. Noting that the face normals in the divergence theorem point in opposite directions on opposite faces, Equation (12) can be approximated using the discrete mesh values as:

$$\begin{aligned}\rho u_e u_e \Delta y_e - \rho u_w u_w \Delta y_w + \rho v_n u_n \Delta x_n - \rho v_s u_s \Delta x_s &= -(p_e \Delta y_e - p_w \Delta y_w) + \\ \mu \frac{u_{i+1, j} - u_{i, j}}{\Delta x_e} - \mu \frac{u_{i, j} - u_{i-1, j}}{\Delta x_w} + \mu \frac{u_{i, j+1} - u_{i, j}}{\Delta y_n} - \mu \frac{u_{i, j} - u_{i, j-1}}{\Delta y_s}\end{aligned}\quad (13)$$

One aspect of using a staggered mesh arrangement is that there isn't a consistent (i, j) indexing of the $\mathcal{M}_u, \mathcal{M}_v$ and \mathcal{M}_p meshes. In Equation (13) the (i, j) indices refer to the \mathcal{M}_u mesh and the v and p values are labelled according to their cardinal positions on the u -momentum control volume.

The terms such as $u_e u_e$ in Equation (13) are non-linear terms. In the SIMPLE algorithm these are treated using a fixed point iteration, also known as a Picard iteration, where the product $u_e u_e$ is separated into a *convecting* velocity and a

convected velocity. The *convecting* velocity is fixed based on the current solution field and the discrete equations are used to solve for an updated *convected* velocity. The convention in the SIMPLE method is to label the updated velocity with an asterisk. As Appendix A.4 will show these velocities are interim solutions within an overall predictor-corrector algorithm.

Whilst the Δx and Δy do not vary across a given control volume, the mesh spacing may be non-uniform meaning, for example, that $\Delta x_e \neq \Delta x_w$. However, for notational simplicity, Δx and Δy can be taken as constants. Hence, applying the fixed point iteration to Equation (13) gives:

$$\begin{aligned} \frac{1}{2}\rho u_e (u_{i,j}^* + u_{i+1,j}^*) \Delta y - \frac{1}{2}\rho u_w (u_{i,j}^* + u_{i-1,j}^*) \Delta y + \\ \frac{1}{2}\rho v_n (u_{i,j}^* + u_{i,j+1}^*) \Delta x - \frac{1}{2}\rho v_s (u_{i,j}^* + u_{i,j-1}^*) \Delta x = \\ -(p_e^* - p_w^*) \Delta y + \\ \mu \frac{u_{i+1,j}^* - 2u_{i,j}^* + u_{i-1,j}^*}{\Delta x} + \mu \frac{u_{i,j+1}^* - 2u_{i,j}^* + u_{i,j-1}^*}{\Delta y} \end{aligned} \quad (14)$$

The *convecting* velocities u_e, u_w, v_n and v_s have not been expanded as this requires certain stability considerations to be taken into account. These are described fully in sections 5.6 and onwards of [6]. For simplicity, this work used the 1st order upwinding scheme.

The terms in Equation (14) can be collected together to give the discrete u -momentum equation:

$$a_P^u u_{i,j}^* = a_E^u u_{i+1,j}^* + a_W^u u_{i-1,j}^* + a_N^u u_{i,j+1}^* + a_S^u u_{i,j-1}^* - (p_e^* - p_w^*) \Delta y \quad (15)$$

The subscripts on the coefficients a^u are capitalised to indicate they correspond to nodes in the mesh \mathcal{M}_u . Using nb to denote the cardinal neighbours, Equation (15) can be simplified to:

$$a_P^u u_{i,j}^* = \sum_{nb} a_{nb}^u u_{nb}^* - (p_e^* - p_w^*) \Delta y \quad (16)$$

Following the same steps on mesh \mathcal{M}_v , the discrete v -momentum equation is:

$$a_P^v v_{i,j}^* = \sum_{nb} a_{nb}^v v_{nb}^* - (p_n^* - p_s^*) \Delta x \quad (17)$$

Equations (16) to (17) illustrate the main reason for using a staggered mesh which is that the pressure gradients in each equation are computed using the difference between adjacent pressure values in the \mathcal{M}_p mesh. This avoids a pressure-velocity decoupling that can create a spurious checkerboard pattern in the pressure field [49].

A.3 Mass conservation equation

Equations (16) to (17) can be solved using a number of iterative schemes for u^* and v^* with fixed values for p^* . The next step in the SIMPLE algorithm is to use the mass conservation equation to *correct* the velocities and pressure by:

$$\begin{aligned} u &= u^* + u' \\ v &= v^* + v' \\ p &= p^* + p' \end{aligned} \quad (18)$$

The corrections should produce a solution that satisfies the discrete momentum equations and since the starred variables already do so, substituting Equation (18) into Equations (16) to (17) produces:

$$\begin{aligned} a_P^u u'_{i,j} &= \sum_{nb} a_{nb}^u u'_{nb} - (p'_e - p'_w) \Delta y \\ a_P^v v'_{i,j} &= \sum_{nb} a_{nb}^v v'_{nb} - (p'_n - p'_s) \Delta x \end{aligned} \quad (19)$$

Note that the updates are part of an overall iterative scheme where in the converged solution: $|u'|, |v'|, |p'| < \epsilon_{tol}$ with ϵ_{tol} being a small number close to machine precision. Hence the sums of neighbours in Equation (19) can be

ignored knowing that in the converged solution they will be close to zero, Replacing the the cardinal references for p with the mesh indexing as shown Figure 15c yields:

$$\begin{aligned} u_{i,j} &= u_{i,j}^* - \frac{\Delta y}{a_{i,j}^u} (p'_{i,j} - p'_{i-1,j}) \\ v_{i,j} &= v_{i,j}^* - \frac{\Delta x}{a_{i,j}^v} (p'_{i,j} - p'_{i,j-1}) \end{aligned} \quad (20)$$

Discretising the mass conservation equation using the divergence theorem gives:

$$\rho(u_{i+1,j} - u_{i,j})\Delta y + \rho(v_{i,j+1} - v_{i,j})\Delta x = 0 \quad (21)$$

Substituting u and v from Equation (20) into Equation (21) gives an equation of the form

$$a_{P'}^p p'_{i,j} = \sum_{nb} a_{nb}^p p'_{nb} - \rho ((u_{i+1,j}^* - u_{i,j}^*)\Delta y + (v_{i,j+1}^* - v_{i,j}^*)\Delta x) \quad (22)$$

The term involving u^* and v^* on the RHS of Equation (22) can be seen to be the deficit by which the solution of the momentum equations satisfies the continuity equations, usually referred to as the residual error or just residual. If the continuity residual is zero, then $p' = 0$ and both the momentum and mass conservation equations have been solved.

A.4 The SIMPLE algorithm

Before summarising the SIMPLE algorithm, the notation is changed to use the Dirac *bra-ket* notation. Let $|u\rangle$ be the vector of $u_{i,j}$ velocities $\forall (i,j) \in \mathcal{M}_u$, Similarly for $|v\rangle$, $|p\rangle$ and the \mathcal{M}_v , \mathcal{M}_p meshes respectively. The point-wise discretisation equations for u^* and v^* from Equations (16) to (17) and the continuity Equation (22) for every node in their meshes can be written as matrix equations:

$$\begin{aligned} A^u |u^*\rangle &= D^x |p^*\rangle \\ A^v |v^*\rangle &= D^y |p^*\rangle \\ A^p |p'\rangle &= M^x |u^*\rangle + M^y |v^*\rangle \end{aligned} \quad (23)$$

where the entries in matrices A^u , A^v and A^p contain linearised terms depending on $|u\rangle$, $|v\rangle$ and $|p\rangle$. The matrices D^x and D^y depend only on the mesh coordinates; and M^x and M^y depend on the mesh coordinates and the constant density. Algorithm 1 gives the full SIMPLE method.

Algorithm 1: SIMPLE (Semi-Implicit Method for Pressure Linked Equations)

Result: Solution $|u\rangle$, $|v\rangle$ and $|p\rangle$ to the 2D mass and momentum equations

Set initial values for $|u\rangle$, $|v\rangle$ and $|p\rangle$;

converged $\leftarrow 0$;

while While converged $\neq 0$ **do**

 set A^u and A^v from ρ , $|u\rangle$, $|v\rangle$ and set $|p^*\rangle \leftarrow |p\rangle$;

 solve;

$A^u |u^*\rangle = D^x |p^*\rangle$ on the mesh \mathcal{M}_u ;

$A^v |v^*\rangle = D^y |p^*\rangle$ on the mesh \mathcal{M}_v ;

 set A^p from A^u and A^v ;

 solve;

$A^p |p'\rangle = M^x |u^*\rangle + M^y |v^*\rangle$ on the mesh \mathcal{M}_p ;

$|u\rangle \leftarrow |u^*\rangle + |u'\rangle$;

$|v\rangle \leftarrow |v^*\rangle + |v'\rangle$;

$|p\rangle \leftarrow |p^*\rangle + |p'\rangle$;

if $\langle u'|u'\rangle, \langle v'|v'\rangle, \langle p'|p'\rangle \leq \epsilon_{tol}^2$ **then**

 converged $\leftarrow 1$;

end

end

A.5 Boundary conditions

There are 2 general classes of boundary conditions used in CFD:

- **Dirichlet** - the value of a variable is prescribed at the boundary.
- **Neumann** - the derivative of a variable is prescribed at the boundary.

These are applied over the set of mesh nodes, $\partial\mathcal{M}_u$, that form the boundary of \mathcal{M}_u . In general, boundaries are topologically defined, e.g. inflow, outflow, wall, and there are multiple nodes on each boundary and multiple boundaries of each type in a CFD calculation. If there are n such boundaries:

$$\partial\mathcal{M}_u = \bigcup_{k=1}^n \partial\mathcal{M}_u^k \quad (24)$$

Where each boundary set $\partial\mathcal{M}_u^k$ contains all the mesh nodes that lie on that boundary and share the same boundary type. In this work, only Dirichlet boundary conditions are used. For example, if node labelled (i, j) is on a solid wall boundary moving with velocity u_{wall} :

$$\begin{aligned} u_{i+1,j}^* &= u_{wall} \\ u'_{i+1,j} &= 0 \end{aligned} \quad (25)$$

In matrix form, the boundary conditions are included as:

$$\begin{aligned} (A^u + B^u)|u^*\rangle &= D^x|p^*\rangle + |u_b\rangle \\ (A^v + B^v)|v^*\rangle &= D^y|p^*\rangle + |v_b\rangle \end{aligned} \quad (26)$$

Where $|u_b\rangle$ and $|v_b\rangle$ have zero amplitudes at the interior nodes and the specified boundary values at the boundary nodes.

The construction of the staggered mesh means that boundary conditions for the pressure are not needed. However, since the pressure only enters the Navier-Stokes equations via its gradients, it is only unique up to an additive constant. To ensure that the solution of the pressure correction remains bounded, Equation (22) is modified at one node in the \mathcal{M}_p mesh, usually the node $(1,1)$, to be:

$$a_{Pp}^p p'_{1,1} = 0 \quad (27)$$

This is achieved by setting all the neighbour coefficients a_{nb}^p to zero at node $(1,1)$.

B Generating a linear combination of unitaries for CFD matrices

As shown in Appendix A CFD algorithms create inner linearised systems that solve an update equation of the form $A|\delta x\rangle = |\delta b\rangle$, where A and $|\delta b\rangle$ depend on $|x\rangle$. After solving the linear system: $|x\rangle \leftarrow |x\rangle + |\delta x\rangle$, A and $|\delta b\rangle$ are updated using the new value of $|x\rangle$ and the process is repeated until $\langle \delta x | \delta x \rangle$ and/or $\langle \delta b | \delta b \rangle$ are below a user specified convergence tolerance. The characteristic feature of this process is that the entries in A change each time $|x\rangle$ is updated but its sparsity pattern does not.

A new method for rapidly recalculating the coefficients in a LCU is discussed in this Appendix. Although the finite volume discretisation scheme used in CFD creates symmetric entries, the boundary conditions add non-symmetric terms. Hence, at each iteration, the linear system to be solved is:

$$\begin{pmatrix} 0 & A \\ A^\dagger & 0 \end{pmatrix} \begin{pmatrix} 0 \\ \delta x \end{pmatrix} = \begin{pmatrix} \delta b \\ 0 \end{pmatrix} \quad (28)$$

Which requires a unitary decomposition of the form:

$$H = \sum_{i=1}^M \alpha_i U_i \quad (29)$$

Since, the focus of this study is CFD matrices only real valued matrices are considered. We also assume that there are few, if any, repeated entries in a CFD matrix other than pairwise symmetric entries.

B.1 Entry-wise decomposition

A straightforward approach is to use each pair of symmetric entries in H as the basis for a pair of 1-sparse unitaries. If $h_{i,j} = h_{j,i}$ are the symmetric pair, initialise two unitaries with unit entries at the same locations. A simple marching algorithm can then add 1 to each remaining row and column of one of the unitaries and -1 to the second. The coefficient for each unitary is $\frac{1}{2}h_{i,j}$. This is illustrated in Equation (30)

$$\begin{pmatrix} 0 & 0 & 0 & 0 \\ 0 & 0 & 0.4 & 0 \\ 0 & 0.4 & 0 & 0 \\ 0 & 0 & 0 & 0 \end{pmatrix} = 0.2 \begin{pmatrix} 1 & 0 & 0 & 0 \\ 0 & 0 & 1 & 0 \\ 0 & 1 & 0 & 0 \\ 0 & 0 & 0 & 1 \end{pmatrix} + 0.2 \begin{pmatrix} -1 & 0 & 0 & 0 \\ 0 & 0 & 1 & 0 \\ 0 & 1 & 0 & 0 \\ 0 & 0 & 0 & -1 \end{pmatrix} \quad (30)$$

This approach is the most efficient in terms of re-evaluating the coefficients of the unitaries as there is a direct 1-1 correspondence between the coefficients and the entries in the CFD matrix. However, there is some arbitrariness in the creation of unitaries and not all are guaranteed to produce efficient circuit implementations. Similar methods are more effective on matrices with many repeated entries. [31] used a 1-dimensional colouring scheme to decompose a tri-diagonal Toeplitz matrix into three 1-sparse matrices with non-integer coefficients. [50] decomposed dense circulant matrices into a sum of 1-sparse matrices each of which corresponded to one of the repeated coefficients in the circulant matrix. Circuits were written in terms of the unitaries and not further decomposed. [29] provided circuits for a number of 1-sparse Hamiltonians including those with real valued entries. However, these circuits required n ancilla qubits in addition the n qubits on which the Hamiltonian operated.

For circuit optimisation, it is preferable to decompose the Hamiltonian into unitaries that are products of the Pauli operators such as in the Jordan-Wigner transformation used to relate Pauli strings with Fermionic operators in quantum chemistry [51]. However, CFD matrices do not have a Fermionic basis and an alternative method of creating Pauli strings is needed. Note that the matrix in Equation (30) can alternatively be decomposed into: $0.2X \otimes X + 0.2Y \otimes Y$.

B.2 Decomposition using trace orthogonality of Pauli matrices

If each unitary in Equation (29) is a product of Pauli matrices, each can be written as:

$$U_i = \bigotimes_{j=1}^n P_{i,j} \quad (31)$$

where $n = \log_2(N)$ is the number of qubits needed for the unitary register, N is the rank of H assumed to be a power of 2 and $P_{i,j} \in \{I, X, Y, Z\}$ is one of the Pauli matrices (extended to include the identity matrix):

$$\begin{aligned} I &= \begin{pmatrix} 1 & 0 \\ 0 & 1 \end{pmatrix} \\ X &= \begin{pmatrix} 0 & 1 \\ 1 & 0 \end{pmatrix} \\ Y &= \begin{pmatrix} 0 & -i \\ i & 0 \end{pmatrix} \\ Z &= \begin{pmatrix} 1 & 0 \\ 0 & -1 \end{pmatrix} \end{aligned} \quad (32)$$

The number of possible combinations of Pauli matrices is 4^n , or N^2 , i.e. the number of entries in H if it were fully populated.

Trace orthogonality of Pauli matrices arises from the condition:

$$\frac{1}{2} \text{Tr}(P_i P_j) = \delta_{ij} \quad (33)$$

Since $\text{Tr}(A \otimes B) = \text{Tr}(A)\text{Tr}(B)$ and $(A \otimes B)(C \otimes D) = (AC) \otimes (BD)$ trace orthogonality extends to products of Pauli matrices:

$$U_i U_j = \left(\bigotimes_{l=1}^n P_{i,l} \right) \left(\bigotimes_{m=1}^n P_{j,m} \right) = \bigotimes_{l=1}^n P_{i,l} P_{j,l} \quad (34)$$

Giving,

$$\text{Tr}(U_i U_j) = \prod_{l=1}^n \text{Tr}(P_{i,l} P_{j,l}) = 2^n \prod_{l=1}^n \delta_{i_l j_l} \quad (35)$$

Hence each coefficient in a unitary expansion based on Pauli strings can be found using:

$$\alpha_i = \frac{1}{2^n} \text{Tr}(U_i H) \quad (36)$$

Calculating which unitaries are in the decomposition notionally requires all N^2 Pauli products to be checked. Care is needed on the initial set-up to ensure starting values which happen to be equal do not cause unitaries to be omitted that would have non-zero coefficients in later iterations.

Re-evaluating the LCU coefficients is a simple matter of reapplying Equation (36) using the stored unitaries. Using 64-bit integers and double precision reals this requires $3MN \times 8$ bytes of storage. This is independent of the sparse storage format as they all have to store the row, column and value of each 1-sparse entry. For this study, storing the unitaries is not an issue and provides a like-with-like comparison with the method that has been developed and will be described next.

B.3 Decomposition using Hadamard based orthogonality of Pauli matrices

In this work, an alternative form of orthogonality has been developed based on the grand sum of Hadamard products [52]. The Hadamard product, denoted by \circ , is the element-wise product of 2 matrices of the same shape. For example:

$$\begin{pmatrix} a & b \\ c & d \end{pmatrix} \circ \begin{pmatrix} e & f \\ g & h \end{pmatrix} = \begin{pmatrix} ae & bf \\ cg & dh \end{pmatrix}$$

More generally, if A and B have the same shape:

$$(A \circ B)_{ij} = A_{ij} B_{ij} \quad (37)$$

From Equation (32) and Equation (37), the Hadamard products of the Pauli matrices can be calculated as shown in Table 9.

\circ	I	X	Y	Z
I	I	0	0	Z
X	0	X	Y	0
Y	0	Y	-X	0
Z	Z	0	0	I

Table 9: Hadamard products of the Pauli matrices. Note that 0 is the 2x2 null matrix with all zero entities.

Define G as the *grand sum* of all the elements in a matrix:

$$G(A) = \sum_{i,j} A_{i,j} \quad (38)$$

And G_H the grand sum of a Hadamard product:

$$G_H(A, B) = G(A \circ B) = \sum_{i,j} A_{i,j} B_{i,j} \quad (39)$$

Applying G_H to the Hadamard products in Table 9 gives:

G_H	I	X	Y	Z
I	2	0	0	0
X	0	2	0	0
Y	0	0	-2	0
Z	0	0	0	2

Table 10: Grand sum of Hadamard products of the Pauli matrices.

As Table 10 shows, G_H provides an orthogonal operator for Hadamard products of Pauli matrices. As will be shown later, under the conditions of a typical CFD matrix, this can be extended to provide orthonormality.

From their definitions, Hadamard and Kronecker products are related by:

$$(A \otimes B) \circ (C \otimes D) = (A \circ C) \otimes (B \circ D) \quad (40)$$

By construction:

$$G(A \otimes B) = G(A)G(B) \quad (41)$$

Hence:

$$G_H(A \otimes B, C \otimes D) = G_H(A, C)G_H(B, D) \quad (42)$$

B.3.1 Sparsity considerations

Let S_H denote the sparsity pattern of the symmetrised CFD matrix and S_U denote the sparsity pattern of the sum of unitaries in Equation (29). Since, the objective of the methodology is to re-use the same set of unitaries for matrices with different entries during the CFD solution process, the decomposition must ensure that $S_H \cap S_U = S_H$. In general, the relative complement $S_U - S_H$ is not an empty set and contains some of the zero entries in H that are not stored in its sparse matrix representation. The solution of Equation (29) must ensure these entries are zero. To do this, the sparse matrix representation of H is in-filled with the zero entries to create an expanded matrix \hat{H} such that $S_U - S_{\hat{H}} = \{\}$. Equation (29) can be restated as:

$$\hat{H} = \sum_{i=1}^{\hat{M}} \alpha_i U_i \quad (43)$$

Mathematically, Equation (29) and Equation (43) are equivalent, the distinction between H and \hat{H} is purely algorithmic due to their different sparsity patterns. Typically, $\hat{M} \geq M$, because the algorithm computes the unitary decomposition

for all possible non-zero entries rather than a specific set of values. For any given sparse matrix, some or many of the α_i values in Equation (43) may be zero.

A second sparsity consideration is that I and Z, and X and Y have the same sparsity patterns. It is easy to see that in the set of all n qubit tensor products of Pauli matrices, there are subsets of size $N = 2^n$ that have the same sparsity pattern. Since all products of Pauli matrices are *1-sparse*, the number of non-zero entries in each product is also N . The intersection of any 2 subsets is the empty set, i.e. the subsets have non-overlapping sparsity patterns that fill a square matrix of rank N . This can be seen by the fact that such a matrix has N^2 entries which is the same as the number of subsets times the number of non-zero entries in the shared sparsity pattern of each set. If the sparsity pattern of two subsets overlapped, there would be at least one position in the matrix not included in any of the sparsity subsets.

B.3.2 Solving for the unitary coefficients

Rather than solve for the complete set of unitaries, it is more efficient to solve for each subset. Since all the elements of a subset share a common sparsity pattern, the subsets are called clusters. Each cluster contains M unitaries each with N non-zero entries. Applying the *vec* operator to the non-zero entries in each unitary gives:

$$\begin{pmatrix} \hat{H}_1 \\ \hat{H}_2 \\ \vdots \\ \hat{H}_N \end{pmatrix} = \begin{pmatrix} U_{1,1} & U_{2,1} & \dots & U_{M,1} \\ U_{1,2} & U_{2,2} & \dots & U_{M,2} \\ \vdots & \vdots & \ddots & \vdots \\ U_{1,N} & U_{2,N} & \dots & U_{M,N} \end{pmatrix} \begin{pmatrix} \alpha_1 \\ \alpha_2 \\ \vdots \\ \alpha_M \end{pmatrix} \quad (44)$$

Equation (44) uses a local indexing following the sparse storage method of the matrices, e.g. compressed row, compressed column, etc. In this equation $U_{i,j}$ denotes the j^{th} entry in the i^{th} unitary. It appears that all that has happened is that an $N \times M$ full matrix inversion is needed to solve for the coefficients. However, denoting the matrix of unitaries by U gives:

$$U^T U = \begin{pmatrix} U_{1,1} & U_{1,2} & \dots & U_{1,N} \\ U_{2,1} & U_{2,2} & \dots & U_{2,N} \\ \vdots & \vdots & \ddots & \vdots \\ U_{M,1} & U_{M,2} & \dots & U_{M,N} \end{pmatrix} \begin{pmatrix} U_{1,1} & U_{2,1} & \dots & U_{M,1} \\ U_{1,2} & U_{2,2} & \dots & U_{M,2} \\ \vdots & \vdots & \ddots & \vdots \\ U_{1,N} & U_{2,N} & \dots & U_{M,N} \end{pmatrix} \quad (45)$$

Since all the unitaries have the same sparsity pattern and the omitted entries are all zero, the product of the i^{th} row of U^T and the j^{th} column of U is the grand sum of a Hadamard product:

$$(U^T U)_{ij} = G(U_i \circ U_j) = G_H(U_i, U_j)$$

Using the definition of U from Equation (31) and the identities from Equation (40) and Equation (41) gives:

$$\begin{aligned} (U^T U)_{ij} &= G \left(\bigotimes_{k=1}^n P_{i,k} \circ \bigotimes_{k=1}^n P_{j,k} \right) \\ &= G \left(\bigotimes_{k=1}^n (P_{i,k} \circ P_{j,k}) \right) \\ &= \prod_{k=1}^n G_H(P_{i,k}, P_{j,k}) \end{aligned} \quad (46)$$

Considering $(U^T U)_{ii}$ and using the values from Table 10 gives:

$$(U^T U)_{ii} = \prod_{k=1}^n (\pm 2) = \pm 2^n \quad (47)$$

However, it is only $Y \circ Y$ that results in -2 . If the methodology is restricted to only real-valued CFD matrices, then each U_i must contain an even number of Y matrices and the final product in Equation (46) must contain an even

number of $Y \circ Y$ products. Hence,

$$(U^T U)_{ii} = 2^n, \forall i \quad (48)$$

If $i \neq j$, then since unitaries in the cluster are unique, there must be at least one Hadamard product $P_{i,k} \circ P_{j,k}$ for which two different Pauli matrices are being multiplied. From Table 10, there is at least one $G_H(P_{i,k}, P_{j,k}) = 0$. Hence,

$$(U^T U)_{ij} = 0, \forall i \neq j \quad (49)$$

Combining Equation (48) and Equation (49) gives:

$$U^T U = 2^n I \quad (50)$$

And the coefficients for this cluster can be directly computed from:

$$\begin{pmatrix} \alpha_1 \\ \alpha_2 \\ \vdots \\ \alpha_M \end{pmatrix} = \frac{1}{2^n} \begin{pmatrix} U_{1,1} & U_{1,2} & \dots & U_{1,N} \\ U_{2,1} & U_{2,2} & \dots & U_{2,N} \\ \vdots & \vdots & \ddots & \vdots \\ U_{M,1} & U_{M,2} & \dots & U_{M,N} \end{pmatrix} \begin{pmatrix} \hat{H}_1 \\ \hat{H}_2 \\ \vdots \\ \hat{H}_N \end{pmatrix} \quad (51)$$

Repeating this process for all clusters gives the complete unitary decomposition for H . Storing U^T for each cluster allows the unitary decomposition to be quickly recomputed each time the outer CFD iteration updates the matrix system to be solved.

Note, that in the above derivation M and N do not have to be equal and for symmetrised matrices following Equation (4), the algorithm can be applied to the upper right block of H for which $M = \frac{N}{2}$.

An important computational aspect of this result is that the entries U_{ij} all have values of ± 1 . By letting $0 \mapsto -1$, a single bit, b , can be used to store the each entry such that its value is $-1 + 2b$. In the current implementation, a single byte is used, i.e. `int8_t` in C.

Comparing the storage requirements with the trace orthogonality approach, this method effectively stores all the non-zero entries in the LCU decomposition but not as a set of sparse matrices. The total number of entries stored is MN bytes, using the 1 byte for each entry. Since each cluster shares a sparsity pattern, the sparse matrix indexing needs only be stored once for each cluster, requiring $2n_c N \times 8$ bytes of storage. Since $n_c \ll M$ this is a significant saving in storage relative to the trace orthogonality method.

References

- [1] M. Walport, M. Calder, C. Craig, D. Culley, R. de Cani, C. Donnelly, R. Douglas, B. Edmonds, J. Gascoigne, N. Gilbert, *et al.*, *Computational Modelling: Technological Futures*. Government Office for Science, 2018.
- [2] N. Hills, “Achieving high parallel performance for an unstructured unsteady turbomachinery cfd code,” *The aeronautical journal*, vol. 111, no. 1117, pp. 185–193, 2007.
- [3] L. Lapworth, “Parallel encryption of input and output data for hpc applications,” *The International Journal of High Performance Computing Applications*, p. 10943420211016516, 2021.
- [4] C. Pérez Arroyo, J. Dombard, F. Duchaine, L. Gicquel, N. Odier, G. Exilard, S. Richard, N. Buffaz, and J. Démolis, “Large-eddy simulation of an integrated high-pressure compressor and combustion chamber of a typical turbine engine architecture,” in *Turbo Expo: Power for Land, Sea, and Air*, vol. 84089, p. V02CT35A058, American Society of Mechanical Engineers, 2020.
- [5] A. Gerstenberger, “3d cfd in-situ co-processing for turbomachinery design,” in *ISAV 21: In Situ Infrastructures for Enabling Extreme-Scale Analysis and Visualization*, 2021.
- [6] H. K. Versteeg and W. Malalasekera, *An introduction to computational fluid dynamics: the finite volume method*. Pearson education, 2007.
- [7] R. Steijl, “Quantum algorithms for fluid simulations,” *Advances in Quantum Communication and Information*, p. 31, 2019.
- [8] F. Gaitan, “Finding flows of a navier–stokes fluid through quantum computing,” *npj Quantum Information*, vol. 6, no. 1, pp. 1–6, 2020.
- [9] B. Kacewicz, “Almost optimal solution of initial-value problems by randomized and quantum algorithms,” *Journal of Complexity*, vol. 22, no. 5, pp. 676–690, 2006.
- [10] P. C. Costa, S. Jordan, and A. Ostrander, “Quantum algorithm for simulating the wave equation,” *Physical Review A*, vol. 99, no. 1, p. 012323, 2019.
- [11] A. Suau, G. Staffelbach, and H. Calandra, “Practical quantum computing: solving the wave equation using a quantum approach,” *ACM Transactions on Quantum Computing*, vol. 2, no. 1, pp. 1–35, 2021.
- [12] C. Lu, Z. Hu, B. Xie, and N. Zhang, “Quantum cfd simulations for heat transfer applications,” in *ASME International Mechanical Engineering Congress and Exposition*, vol. 84584, p. V010T10A050, American Society of Mechanical Engineers, 2020.
- [13] A. W. Harrow, A. Hassidim, and S. Lloyd, “Quantum algorithm for linear systems of equations,” *Physical review letters*, vol. 103, no. 15, p. 150502, 2009.
- [14] O. Kyriienko, A. E. Paine, and V. E. Elfving, “Solving nonlinear differential equations with differentiable quantum circuits,” *Physical Review A*, vol. 103, no. 5, p. 052416, 2021.
- [15] M. Lubasch, J. Joo, P. Moinier, M. Kiffner, and D. Jaksch, “Variational quantum algorithms for nonlinear problems,” *Physical Review A*, vol. 101, no. 1, p. 010301, 2020.
- [16] B. Ljubomir, “Quantum algorithm for the navier–stokes equations by using the streamfunction-vorticity formulation and the lattice boltzmann method,” *International Journal of Quantum Information*, p. 2150039, 2022.
- [17] A. C. Vazquez, R. Hiptmair, and S. Woerner, “Enhancing the quantum linear systems algorithm using richardson extrapolation,” *arXiv preprint arXiv:2009.04484*, 2020.
- [18] H. F. Trotter, “On the product of semi-groups of operators,” *Proceedings of the American Mathematical Society*, vol. 10, no. 4, pp. 545–551, 1959.
- [19] M. Suzuki, “General theory of fractal path integrals with applications to many-body theories and statistical physics,” *Journal of Mathematical Physics*, vol. 32, no. 2, pp. 400–407, 1991.
- [20] G. H. Low and I. L. Chuang, “Hamiltonian Simulation by Qubitization,” *Quantum*, vol. 3, p. 163, July 2019.
- [21] A. M. Childs and N. Wiebe, “Hamiltonian simulation using linear combinations of unitary operations,” *arXiv preprint arXiv:1202.5822*, 2012.
- [22] R. Kothari, *Efficient algorithms in quantum query complexity*. PhD thesis, University of Waterloo, 2014.
- [23] D. W. Berry, A. M. Childs, R. Cleve, R. Kothari, and R. D. Somma, “Simulating hamiltonian dynamics with a truncated taylor series,” *Physical review letters*, vol. 114, no. 9, p. 090502, 2015.
- [24] D. W. Berry, M. Kieferová, A. Scherer, Y. R. Sanders, G. H. Low, N. Wiebe, C. Gidney, and R. Babbush, “Improved techniques for preparing eigenstates of fermionic hamiltonians,” *npj Quantum Information*, vol. 4, no. 1, pp. 1–7, 2018.

- [25] R. Babbush, C. Gidney, D. W. Berry, N. Wiebe, J. McClean, A. Paler, A. Fowler, and H. Neven, “Encoding electronic spectra in quantum circuits with linear t complexity,” *Physical Review X*, vol. 8, no. 4, p. 041015, 2018.
- [26] J. M. Martyn, Z. M. Rossi, A. K. Tan, and I. L. Chuang, “Grand unification of quantum algorithms,” *PRX Quantum*, vol. 2, no. 4, p. 040203, 2021.
- [27] A. Gilyén, Y. Su, G. H. Low, and N. Wiebe, “Quantum singular value transformation and beyond: exponential improvements for quantum matrix arithmetics,” in *Proceedings of the 51st Annual ACM SIGACT Symposium on Theory of Computing*, pp. 193–204, 2019.
- [28] Y. Dong, X. Meng, K. B. Whaley, and L. Lin, “Efficient phase-factor evaluation in quantum signal processing,” *Physical Review A*, vol. 103, no. 4, p. 042419, 2021.
- [29] G. R. Ahokas, *Improved algorithms for approximate quantum Fourier transforms and sparse Hamiltonian simulations*. University of Calgary, 2004.
- [30] D. W. Berry, G. Ahokas, R. Cleve, and B. C. Sanders, “Efficient quantum algorithms for simulating sparse hamiltonians,” *Communications in Mathematical Physics*, vol. 270, no. 2, pp. 359–371, 2007.
- [31] A. C. Vázquez, *Quantum Algorithm for Solving Tri-Diagonal Linear Systems of Equations*. PhD thesis, ETH Zürich, 2018.
- [32] A. Scherer, B. Valiron, S.-C. Mau, S. Alexander, E. Van den Berg, and T. E. Chapuran, “Concrete resource analysis of the quantum linear-system algorithm used to compute the electromagnetic scattering cross section of a 2d target,” *Quantum Information Processing*, vol. 16, no. 3, pp. 1–65, 2017.
- [33] R. Kothari, “Efficient simulation of hamiltonians,” Master’s thesis, University of Waterloo, 2010.
- [34] A. M. Childs and R. Kothari, “Simulating sparse hamiltonians with star decompositions,” in *Conference on Quantum Computation, Communication, and Cryptography*, pp. 94–103, Springer, 2010.
- [35] S. Patankar and D. Spalding, “A calculation procedure for heat, mass and momentum transfer in three-dimensional parabolic flows,” *Int. J. Heat Mass Transfer*, vol. 15, pp. 1787–1806, 1972.
- [36] R. E. Smith Jr and A. Kidd, “Comparative study of two numerical techniques for the solution of viscous flow in a driven cavity,” *NASA Special Publication*, vol. 378, p. 61, 1975.
- [37] K. Ghia, W. Hankey, JR, and J. Hodge, “Study of incompressible navier-stokes equations in primitive variables using implicit numerical technique,” in *3rd Computational Fluid Dynamics Conference*, p. 648, 1977.
- [38] S. Shahpar, “Building digital twins to simulate manufacturing variation,” in *Turbo Expo: Power for Land, Sea, and Air*, vol. 84065, p. V02AT32A049, American Society of Mechanical Engineers, 2020.
- [39] I. Z. Reguly and G. R. Mudalige, “Modernising an industrial cfd application,” in *2020 Eighth International Symposium on Computing and Networking Workshops (CANDARW)*, pp. 191–196, IEEE, 2020.
- [40] H. Redal, J. Carpio, P. A. García-Salaberri, and M. Vera, “Dynamfluid: Development and validation of a new gui-based cfd tool for the analysis of incompressible non-isothermal flows,” *Processes*, vol. 7, no. 11, p. 777, 2019.
- [41] R. Bouffanais, M. O. Deville, and E. Leriche, “Large-eddy simulation of the flow in a lid-driven cubical cavity,” *Physics of Fluids*, vol. 19, no. 5, p. 055108, 2007.
- [42] D. A. Shetty, T. C. Fisher, A. R. Chunekar, and S. H. Frankel, “High-order incompressible large-eddy simulation of fully inhomogeneous turbulent flows,” *Journal of computational physics*, vol. 229, no. 23, pp. 8802–8822, 2010.
- [43] G. Courbebaisse, R. Bouffanais, L. Navarro, E. Leriche, and M. Deville, “Time-scale joint representation of dns and les numerical data,” *Computers & fluids*, vol. 43, no. 1, pp. 38–45, 2011.
- [44] B. Gough, *GNU scientific library reference manual*. Network Theory Ltd., 2009.
- [45] I. F. Araujo, D. K. Park, F. Petruccione, and A. J. da Silva, “A divide-and-conquer algorithm for quantum state preparation,” *Scientific Reports*, vol. 11, no. 1, pp. 1–12, 2021.
- [46] M. Mottonen, J. J. Vartiainen, V. Bergholm, and M. M. Salomaa, “Transformation of quantum states using uniformly controlled rotations,” *arXiv preprint quant-ph/0407010*, 2004.
- [47] J. E. Cohen, S. Friedland, T. Kato, and F. P. Kelly, “Eigenvalue inequalities for products of matrix exponentials,” *Linear Algebra and its Applications*, vol. 45, pp. 55–95, 1982.
- [48] D. Ammour and G. J. Page, “The subgrid-scale approach for modeling impingement cooling flow in the combustor pedestal tile,” *Journal of Heat Transfer*, vol. 140, no. 4, 2018.
- [49] F. H. Harlow and J. E. Welch, “Numerical calculation of time-dependent viscous incompressible flow of fluid with free surface,” *The physics of fluids*, vol. 8, no. 12, pp. 2182–2189, 1965.

- [50] S. Zhou and J. Wang, "Efficient quantum circuits for dense circulant and circulant like operators," *Royal Society open science*, vol. 4, no. 5, p. 160906, 2017.
- [51] M. A. Nielsen *et al.*, "The fermionic canonical commutation relations and the jordan-wigner transform," *School of Physical Sciences The University of Queensland*, vol. 59, 2005.
- [52] L. Lapworth, "Determining solutions to a number of linear matrix equations." Patent Application GB2207665.7, filed 25 May 2022.